

1 **Circadian PERIOD proteins regulate TC-DSB repair through**
2 **anchoring to the nuclear envelope.**

3

4 Benjamin Le Bozec¹, Laure Guitton-Sert¹, Sarah Collins¹, Anne-Laure Finoux¹, Charlotte
5 Payrault¹, Jessica Frison¹, Romane Carette¹, Vincent Rocher¹, Emmanuelle Guillou¹, Coline
6 Arnould¹, Aude Guénolé¹, Marion Aguirrebengoa², Ikrame Lazar¹, Aline Marnef¹, Philippe
7 Frit^{3,4}, Patrick Calsou^{3,4}, Thomas Mangeat⁵, Nadine Puget^{1*} and Gaëlle Legube^{1,6*}

8

9 1. *MCD, Centre de Biologie Intégrative (CBI), CNRS, Université de Toulouse, UT3, 31062*
10 *Toulouse, France*

11 2. *BigA, NGS data analysis facility, Centre de Biologie Intégrative (CBI), CNRS,*
12 *Université de Toulouse, UT3, 31062 Toulouse, France*

13 3. *Institut de Pharmacologie et de Biologie Structurale (IPBS), Université de Toulouse,*
14 *CNRS, Université Toulouse III - Paul Sabatier (UT3), Toulouse, France*

15 4. *Equipe Labellisée Ligue Contre le Cancer 2018, Toulouse, France*

16 5. *LITC Core Facility, Centre de Biologie Intégrative (CBI), CNRS, Université de*
17 *Toulouse, UT3, 31062 Toulouse, France*

18 6. *Lead author*

19

20 * Corresponding authors: gaelle.legube@univ-tlse3.fr, nadine.puget1@univ-tlse3.fr

21 **Running title:** Circadian regulation of TC-DSB repair

22 **Abstract**

23 **Repair of DNA Double-Strand Breaks (DSBs) produced in transcriptionally active**
24 **chromatin occurs through a poorly characterized pathway called Transcription-Coupled**
25 **DSB repair (TC-DSBR). Here, using a screening approach scoring multiple outputs in**
26 **human cells, we identified proteins from the PERIOD complex, a key module ensuring**
27 **circadian oscillations, as novel TC-DSBR players. We show that the core PER complex**
28 **protein PER2 is recruited at TC-DSBs and that it contributes to the targeting of TC-DSBs**
29 **at the nuclear envelope (NE). At the NE, SUN1 and the Nuclear Pore Complex (NPC) act**
30 **as docking sites for TC-DSBs and TC-DSB anchoring fosters RAD51 assembly. Impaired**
31 **DSB localization at the NE results in elevated DSB clustering and translocation rate. In**
32 **agreement, the circadian clock regulates TC-DSB anchoring to the NE, RAD51 assembly,**
33 **and DSB clustering. Our study shows that DSB localization to the NPC is a conserved**
34 **molecular pathway that also occurs in human cells and provides a direct link between the**
35 **circadian rhythm and the response to DSBs occurring in active genes. This opens new**
36 **therapeutic strategies for chemotherapies based on drugs that are inducing DSBs in active**
37 **loci such as topoisomerase poisons.**

38

39

40 **Main**

41 DNA Double-Strand breaks (DSBs) are among the most toxic lesions that occur on the genome,
42 given their potential to elicit large chromosomal rearrangements. While global genome DSB
43 repair (GG-DSBR) mechanisms have been well characterized, a transcription-coupled arm of
44 DSB repair (TC-DSBR) has only recently been identified¹. Yet, physiological DSBs mostly
45 appear in transcriptionally active loci (TC-DSBs)²⁻⁵ and topoisomerase II inhibitors, classically
46 used for cancer treatment, mainly induce TC-DSBs^{2,4} emphasizing the need to better understand
47 TC-DSBR mechanisms. TC-DSBR entails the ATM- and DNA-PK-dependent transcriptional
48 repression of damaged genes which is necessary for the initiation of resection^{6,7}. TC-DSBs are
49 preferentially repaired by Homologous Recombination (HR) in G2^{8,9}, while in G1, they are
50 refractory to repair and cluster in large subnuclear structures¹⁰ that we recently identified as
51 being a novel, DSB-induced, chromatin compartment (the D-compartment)¹¹ whose formation
52 enhances translocation frequency and checkpoint activation^{11,12}. Additionally, when occurring
53 on human ribosomal DNA, TC-DSBs are physically relocated at the nucleolar periphery where
54 they contact invaginations of the Nuclear Envelope (NE)¹³. Whether localization to the NE also
55 occurs when DSBs arise within RNAPII-transcribed loci is yet unknown, although NE targeting
56 of other types of persistent DSBs and collapsed replication forks have been reported in
57 *Drosophila* and *S. Cerevisiae*¹⁴⁻¹⁹. Altogether the TC-DSBR pathway is still poorly understood.

58

59 **Multi-output screen to identify new TC-DSBR factors**

60 In search of novel TC-DSBR players, we performed a siRNA library screen scoring
61 multiple outputs in the well-characterized human DIvA cell line (Fig. 1a). In this cell line,
62 annotated DSBs are induced throughout the genome in a temporally controlled manner, thanks
63 to a restriction enzyme fused to the ligand binding domain of the estrogen receptor (AsiSI-

64 ER)²⁰. BLESS experiments (enabling mapping and quantification of DSBs throughout the
65 genome using streptavidin-capture and sequencing of fragments adjacent to DSBs ligated to
66 biotinylated linkers²¹) allowed to identify 174 sites robustly cleaved *in vivo* out of the 1211
67 AsiSI sites annotated on the human genome (mainly due to the fact that AsiSI activity is
68 inhibited by DNA methylation)^{20,22}. A large fraction of these DSBs occur in RNAPII-enriched
69 (transcribed) loci hereafter called TC-DSBs^{20,22}. The siRNA library comprised 130 candidate
70 proteins previously identified to be associated with the SMC1 subunit of the cohesin complex,
71 which was previously shown to be recruited at DSBs post-DSB induction¹³. The screen was
72 designed to quantify the effect of candidate protein depletion on 1) γ H2AX foci intensity using
73 high-content imaging, 2) cell survival using a cell proliferation assay, 3) chromosome
74 rearrangement frequency using quantitative PCR and 4) DSB clustering using high content
75 microscopy (Fig. 1a, Extended Data Fig. 1a). A positive control siRNA against SETX, an R-
76 loop resolving factor previously reported to be involved in TC-DSBR^{23,24}, triggered an expected
77 increase in γ H2AX foci intensity, translocation frequency and DSB clustering as well as
78 decreased cell proliferation (Fig. 1b red label, Extended Data Fig. 1b-e). We further validated
79 our screening dataset with the candidate protein Periphilin (PPHLN1, Fig. 1b green label,
80 Extended Data Fig. 1b-e), an H3K9me3 reader of the HUSH complex that we previously
81 reported to be involved in the repair of DSB occurring on ribosomal DNA¹³. In agreement with
82 the screen results (Fig. 1b), depletion of PPHLN1 triggered an increase in γ H2AX foci intensity
83 (Extended Data Fig. 1f-g). We further used a degradable version of AsiSI-ER (AID-tagged
84 DIVA cell line⁸) to measure clonogenic potential and repair post-DSB induction. PPHLN1
85 depletion increased two distinct translocation events and cell death, in agreement with our
86 screen results (Extended Data Fig. 1h-i).

87 Importantly, two-parameter correlations established that γ H2AX intensity was inversely
88 correlated with cell survival but positively correlated with translocation frequency (Fig. 1d-e),

89 consistent with a decreased repair capacity respectively impairing cell proliferation and
90 promoting genome rearrangements. Moreover, increased DSB clustering positively correlated
91 with translocation frequency (Fig. 1f), and increased translocation frequency inversely
92 correlated with cell survival (Fig. 1g) in agreement with previous work^{11,12}. Altogether, results
93 from our siRNA screen establish that TC-DSBR deficiency severely affects cell survival and
94 further confirm the relationship between DSB clustering and genome rearrangements as
95 recently reported^{12,25}.

96

97 **The circadian clock PERIOD proteins contribute to TC-DSB repair.**

98 Hierarchical clustering identified two groups displaying statistically significant
99 differences in clustering, translocation, γ H2AX and cell survival (Fig. 1b-c). Interestingly,
100 among the candidate proteins whose depletion gave similar phenotypes to SETX (*i.e.*, increased
101 γ H2AX staining, decreased cell survival, increased chromosomal rearrangement and increased
102 DSB clustering, Group 1, Fig. 1b-c, Extended Data Fig. 1b-e), we found NONO, SFPQ and
103 DDX5 which all belong to the same complex, the mammalian PERIOD (PER) complex
104 involved in the regulation of the circadian rhythm²⁶⁻²⁹. Similar outputs were also seen for
105 another candidate, the DDX5-paralog DDX17, both DDX5 and DDX17 being human orthologs
106 of the *Neurospora* PRD1 protein involved in circadian rhythmicity³⁰ and existing as a
107 heterodimer³¹. The circadian clock is molecularly controlled by the BMAL1/CLOCK
108 transcriptional activator complex, which regulates the transcription of thousands of genes.
109 Among those, the PER-CRY transcriptional repressor can downregulate BMAL1/CLOCK
110 activity, creating a negative transcriptional feedback loop that ensures circadian oscillations³².
111 In order to directly investigate whether the core clock components of the PER complex play a
112 role in TC-DSBR, we depleted PER1 and PER2 proteins (Extended Data Fig. 2a). As found for

113 DDX17, NONO, DDX5 and SETX (Fig. 1b; Extended Data Fig. 1b), PER1 and PER2
114 knockdown increased γ H2AX foci intensity following DSB induction in DIvA cells (Fig. 2a)
115 with no major changes in cell cycle distribution (Extended Data Fig. 2b). In agreement, PER2-
116 depleted cells also displayed elevated γ H2AX levels around DSBs as detected by chromatin
117 immunoprecipitation (ChIP) (Fig. 2b). In order to validate this finding in another, non-
118 cancerous, cell line, we further depleted PER1 and PER2, alone or in combination, in hTERT
119 RPE-1 cells (RPE1) stably infected with a mAID-AsiSI-ER lentiviral construct (RPE-DIvA).
120 PER1 and/or PER2 depleted cells displayed elevated γ H2AX levels post DSB induction by
121 AsiSI (Extended Data Fig. 2c-d). Moreover, γ H2AX increase following PER1/2 depletion also
122 hold true when inducing DSB using etoposide, a Topoisomerase 2 (TOP2) inhibitor known to
123 mainly trigger DSBs in transcribed loci and regulatory elements^{2,4} (Extended Data Fig. 2e). Of
124 note in RPE1 cells, PER1/2 depletion also significantly increased γ H2AX levels even before
125 DSB induction using AsiSI or etoposide (Extended Data Fig. 2c-e), suggesting that PER1/2
126 contribute to endogenous DSB repair.

127 As found for DDX17, NONO, SETX and DDX5 (Fig. 1b; Fig. 2c-d; Extended Data Fig. 1c-d;
128 Extended Data Fig. 2g-i), PER1 and PER2 depletion increased translocation frequency (Fig.
129 2c) and impaired cell survival following induction of TC-DSBs in DIvA cells (Fig. 2d;
130 Extended Data Fig. 2f). Concomitant depletion of PER1 and PER2 triggered exacerbated
131 translocation frequency and cell death following DSB induction, as compared to PER1 or PER2
132 depletion alone (Extended Data Fig. 2h-i). PER1/2 depletion also impaired cell survival upon
133 treatment with the TOP2 inhibitors etoposide and doxorubicin in U2OS and RPE1 (Extended
134 Data Fig. 2j-k).

135 In contrast and surprisingly, depletion of CRY2, known to function in the PER complex, did
136 not result in an elevated translocation rate nor increased cell death (Extended Data Fig. 2h-i).

137 Similarly, depletion of neither BMAL1 nor CLOCK transcriptional activators, alone or in
138 combination, altered the translocation frequency or cell survival post DSB induction (Fig. 2c-
139 d, Extended Data Fig. 2h-i). Altogether, these data show that the PERIOD proteins PER1 and
140 PER2, as well as some other members of the PER complex (NONO, DDX17, SETX and
141 DDX5), contribute to the response to DSBs induced in transcribed loci.

142 In order to determine whether the function of the PER complex is direct, we assessed the
143 recruitment of PER complex proteins at DSBs using ChIP. PER2, DDX17 and DDX5 showed
144 significant recruitment at a TC-DSB induced in DIvA cells (already observed for DDX5³³),
145 while this was not the case for BMAL1 (Fig. 2e). We further performed ChIP-seq against PER2
146 and BMAL1 in damaged and undamaged DIvA cells. Both proteins displayed the expected
147 pattern on the genome (see examples Extended Data Fig. 3a). Indeed, in absence of DSB
148 induction, BMAL1 was enriched on genomic loci previously identified by BMAL1 ChIP-seq³⁴
149 (Extended Data Fig. 3b) and PER2 accumulated at promoters (Extended Data Fig. 3c) as
150 expected for a transcriptional repressor and from previous studies³⁵. Moreover, BMAL1-bound
151 genes displayed significant enrichment for the “rhythmic process” GO term (Extended Data
152 Fig. 3d). Post-DSB induction, we interestingly observed that PER2 accumulated at TC-DSBs
153 (see an example Fig. 2f top panel, purple track) but not at a silent locus (Fig. 2f bottom panel),
154 despite equivalent cleavage (BLESS tracks). In contrast, BMAL1 showed no accumulation at
155 DSBs (Fig. 2f, blue tracks). On average, PER2 was significantly targeted on ~2kb around DSBs,
156 while BMAL1 was not (Fig. 2g, Extended Data Fig. 3e). In agreement with our above data
157 showing that PER1/2 depletion triggers increased γH2AX even before DSB induction
158 (Extended Data Fig. 2c-e), we also observed a significant enrichment of PER2 at previously
159 determined endogenous DSB hotspots¹¹ (Extended Data Fig. 3f). We previously identified a
160 subset of equivalently cleaved DSBs in DIvA cells with two distinct repair behaviors: the Non-
161 Homologous End-Joining (NHEJ)-prone DSBs and the HR-prone DSBs with the latter having

162 a tendency to locate within transcriptionally active loci (*i.e.* TC-DSBs)^{8,22}. Importantly, PER2
163 preferentially accumulates at HR-prone TC-DSBs compared to NHEJ-prone DSBs (*i.e.*
164 occurring in non-transcribed regions) (Fig. 2h). Altogether these data show that the PER
165 complex is recruited at HR-repaired, TC-DSBs, suggesting a direct role of the PER complex in
166 TC-DSB repair.

167

168 **TC-DSBs are targeted to the nuclear envelope via a PER2 -dependent mechanism.**

169 Of interest, the nuclear envelope (NE) contributes to the regulation of the circadian clock³⁶ and
170 PER proteins have been involved in the physical targeting of clock-regulated genes to the NE
171 in *Drosophila*³⁷. On another hand, persistent DSBs^{14,17,38-40}, sub-telomeric DSBs^{41,42},
172 dysfunctional telomeres^{43,44} and arrested replication forks^{18,19} have been previously found to be
173 relocated at the NE in yeast as were stressed replication forks in mammals⁴⁵ and
174 heterochromatic (HC) DSBs in *Drosophila* in order to complete HR^{15,46}. While in mammalian
175 cells, physical relocation of DSBs to the NE has not yet been documented, we previously
176 observed that ribosomal DNA DSBs can contact NE invaginations inside the nucleoplasm¹³.
177 Hence, we set out to determine whether TC-DSBs could be targeted to the NE. As a first
178 approach, we performed fixed and live super-resolution imaging using Random Illumination
179 Microscopy (RIM)⁴⁷. We observed that γ H2AX foci can establish close contacts with LaminB1
180 filaments (Extended data Fig. 4a). Live imaging after 1 hour of DSB induction in DIvA cells
181 expressing 53BP1-GFP and mCherry-LaminB1, showed that such relocalization of DSBs to the
182 nuclear lamina were fast (<60s) and transient (Fig. 3a and Supplementary Videos 1-4). Contacts
183 between repair foci and the nuclear lamina were further confirmed by Proximity Ligation Assay
184 (PLA) performed between LaminB1 and 53BP1 (Fig. 3b) or between γ H2AX and LaminB1
185 (Extended Data Fig. 4b). DSBs induced by etoposide in U2OS cells also displayed interactions

186 with LaminB1 (Extended data Fig. 4c). Moreover, we could recapitulate DSB/LaminB1
187 interactions in RPE1 primary cells subjected to AsiSI or etoposide induced DSBs (Extended
188 data Fig. 4d-e). In agreement, ChIP against LaminB1 (Extended Data Fig. 4f) also revealed
189 increased LaminB1 occupancy at TC-DSBs in contrast to a DSB induced in a silent locus and
190 repaired by NHEJ, in DIvA cells post-DSB induction (Fig. 3c). Taken together, these data
191 suggest that TC-DSBs can be physically relocated at the NE in human cells.

192 In order to evaluate the function of PER2 in targeting TC-DSB at the NE, we performed
193 LaminB1 ChIP in DIvA cells upon PER2 siRNA. Of interest PER2 depletion abolished
194 LaminB1 recruitment at TC-DSBs (Fig. 3d). Additionally, PER1 or PER2-depleted cells also
195 displayed decreased 53BP1/LMNB1 PLA signal post-DSB induction when compared to
196 PER1/2-proficient cells (siRNA CTRL) (Fig. 3e, Extended Data Fig. 4g). Similarly, PER1/2
197 depletion also decreased γ H2AX/LMNB1 PLA signal in response to etoposide (Extended Data
198 Fig. 4h). In order to investigate a potential cell cycle dependency for PER2-mediated DSB
199 anchoring to the NE, we then monitored γ H2AX/LaminB1 PLA signal combined with EdU
200 incorporation by quantitative high throughput microscopy in DIvA cells (Extended Data Fig.
201 4i). PER2 depletion decreased PLA foci in G1, S and G2 cells (Extended Data Fig. 4j).
202 Collectively, these data suggest that PER2 contributes to TC-DSB targeting at the NE.

203

204 **Tethering of TC-DSBs to the NE depends on SUN1 and NUP153**

205 Interestingly, we and others previously reported a function for SUN domain containing-
206 proteins, which are components of the Inner Nuclear Membrane (INM), in DSB mobility in
207 mammals^{10,48}. Moreover, SUN protein orthologs in yeast and *Drosophila* (respectively Mps3,
208 and Koi/Spag4) were also found to act as DSB anchoring points in the NE¹⁵⁻¹⁷. We thus
209 investigated the potential involvement of the two main SUN proteins in mammals, SUN1 and

210 SUN2, in anchoring TC-DSBs to the NE. Interestingly, ChIP against SUN proteins (Extended
211 Data Fig. 5a) revealed that, upon damage, SUN1 displayed enrichment at TC-DSBs compared
212 to NHEJ-DSBs (Extended Data Fig. 5b, top panel). Surprisingly, SUN2 rather showed
213 decreased occupancy post-DSB induction (Extended Data Fig. 5b, bottom panel), suggesting
214 that TC-DSBs are specifically interacting with SUN1 and not SUN2. Of note SUN1 recruitment
215 at TC-DSB was independent of the activity of the three main DNA Damage Response (DDR)
216 kinases, namely ATM, ATR and DNAPK (Extended Data Fig. 5c). To further investigate SUN
217 protein recruitment at DSBs, we performed ChIP-seq against SUN1 and SUN2 before and after
218 DSB induction in DIvA cells. Visual inspection and peak calling on SUN1 and SUN2 ChIP-
219 seq datasets revealed that in undamaged conditions, both proteins are enriched on genes
220 (Extended Data Fig. 5d-e), accumulated at promoters (Extended Data Fig. 5f) and largely
221 overlapped on the genome (Extended Data Fig. 5g). Of interest, post-DSB induction, SUN1
222 (purple track), was recruited on approximately 1kb around the break, while SUN2 rather
223 displayed eviction (blue track) (see an example Fig. 3f top panel, and average profiles at all
224 DSBs Fig. 3g). Both SUN1 recruitment and SUN2 eviction at DSBs were statistically
225 significant when compared to random, undamaged genomic positions (Extended Data Fig. 5h).
226 Notably, the profile of SUN1 at DSBs strongly resembled to that of PER2 (Extended Data Fig.
227 5i), and as PER2, SUN1 also showed enrichment at endogenous DSB hotspots (Extended Data
228 Fig. 5j). Moreover, as observed for PER2, SUN1 was specifically recruited at a TC-DSB (Fig.
229 3f, top panel) but not at a DSB induced in a silent locus (Fig. 3f, bottom panel). On average,
230 SUN1 displayed enhanced accumulation at DSBs with high RNAPII levels compared to those
231 with low RNAPII levels (Extended data Fig. 5k). In agreement, as for PER2, HR-prone DSBs
232 showed higher level of SUN1 as compared to NHEJ-prone DSBs (Extended Data Fig. 5l left
233 panel) while SUN2 depletion was exacerbated at HR-prone DSBs compared to NHEJ-prone
234 DSBs (Extended Data Fig. 5l right panel).

235 We then performed 3D-super resolution imaging by RIM to detect SUN1 and SUN2. Both
236 proteins localized to the NE and displayed punctuated patterns (Extended Data Fig. 6a). Co-
237 staining with γ H2AX enabled the detection of a significant colocalization (ICQ) with SUN1,
238 but not with SUN2 (Extended Data Fig. 6b). Van Steensel Cross-correlation function (CCF)
239 analysis showed a non-random overlap between γ H2AX foci and SUN1 while non-random
240 exclusion was observed between γ H2AX foci and SUN2 (see examples Fig. 3h and
241 quantification Fig. 3i). In agreement with a function of SUN1 in tethering TC-DSB to the NE,
242 depletion of SUN1 (Extended Data Fig. 6c) abolished Lamin B1 enrichment at TC-DSBs (Fig.
243 3j), and also decreased PLA signal between LaminB1 and γ H2AX following etoposide
244 treatment (Extended Data Fig. 6d). Altogether, these data suggest that TC-DSBs are physically
245 targeted to the NE through an interaction with SUN1 and not SUN2.

246 Interestingly, SUN1 has been reported to interact with the Nuclear Pore Complex (NPC), as
247 opposed to SUN2^{49,50}. In agreement, in DIvA cells, we found that SUN1 exhibits significant
248 colocalization with NUP153, a protein part of the NPC basket, as compared to SUN2 (Extended
249 Data Fig. 6e). Given that the NPC has also been identified as a docking site for persistent DSBs
250 and collapsed replication forks in yeast^{14,18,19,38,51} and heterochromatic DSBs in drosophila¹⁵ we
251 thus postulated that the specificity of SUN1 as opposed to SUN2 to anchor DSBs at the NE
252 may be related to its association to the NPC. Indeed, NUP153 accumulates at TC-DSBs but not
253 at a DSB induced in an inactive locus (Extended Data Fig. 6f). 3D-super resolution RIM and
254 CCF analysis further indicated that, as SUN1, NUP153 displays significant colocalization with
255 γ H2AX foci (Fig. 3k, examples on the left panel and quantification on the right panel). Of
256 importance, depletion of NUP153 (Extended Data Fig. 6c) triggered a decreased association of
257 TC-DSB with the NE, as measured by PLA between γ H2AX and LaminB1 (Extended Data Fig.
258 6g), further confirming a function of NUP153 in TC-DSB anchoring. Overall, our data suggest
259 that TC-DSBs are tethered to the NE through a SUN1 and NPC-dependent mechanism.

260

261 **PER2 and SUN1-dependent DSB anchoring at the NPC promotes HR**

262 Given that PER2, SUN1 and NUP153 are recruited at HR-prone DSBs (Fig. 2h, Extended Data
263 Fig. 5l, Extended Data Fig. 6f) and that previous work showed that targeting DSBs and
264 collapsed replication forks to the NPC promotes HR in yeast and drosophila^{14,15,17–19,38,40,46}, we
265 further investigated whether this pathway contributes to HR-repair at TC-DSBs in human cells.
266 One of the first steps of TC-DSB repair is the transcriptional repression of nearby genes
267 (including the damaged gene itself) which is essential for the proper execution of resection and
268 HR repair^{1,52}. Given that the PER complex is a transcriptional repressor, we envisaged that it
269 could promote HR repair at TC-DSBs via a role in transcriptional repression. However, RT-
270 qPCR analyses revealed that both PER2 and PER1 are dispensable for transcriptional repression
271 following DSB induction (Fig. 4a). Similarly, SUN1 depletion did not modify the ability of TC-
272 DSB to trigger transcriptional repression (Fig. 4b) showing that the PER2/SUN1-dependent
273 TC-DSB targeting pathway to the NE is not required for the transcriptional inactivation of genes
274 *in cis* to DSBs. We further investigated the effect of SUN1 and PER1 or PER2 depletion on
275 end-resection, by quantification of single-stranded DNA at DSBs⁵³ (Extended Data Fig. 6h).
276 siRNA depletion of SUN1 did not alter resection (Extended Data Fig. 6i) while both PER1 and
277 PER2 triggered a mild decrease of resection (Extended Data Fig. 6j), although a lot less
278 pronounced than upon CtIP depletion. Altogether, these data suggest that the contribution of
279 NE anchoring in HR repair takes place downstream of transcriptional repression and resection.
280 In drosophila, the targeting of HC breaks to the NE favors RAD51 loading^{15,46}. We thus further
281 assayed in DIVA cells, whether PER2-dependent TC-DSB targeting at the NE regulates RAD51
282 recruitment. Indeed, RAD51 loading at TC-DSBs was significantly reduced in PER2-depleted
283 cells (Fig. 4c). Of interest, in yeast, the eviction of the single strand DNA binding protein RPA,

284 required to ensure Rad51 nucleofilament formation, is promoted by its ubiquitination by the
285 Sumo-Targeted Ubiquitin Ligase (STUbL) Slx5/8¹⁹, which is also required to relocate collapsed
286 forks and DSBs to the NE^{15,18,19,38,40,46}. We thus further tested RPA and RAD51 recruitment at
287 TC-DSBs upon depletion of SUN1 and RNF4, the Slx5/8 ortholog in human cells which has
288 also been previously reported to be involved in HR repair^{54,55}. SUN1 and RNF4 depletion
289 (Extended Data Fig. 6c, Extended Data Fig. 6k) altered the balance between RAD51 and RPA
290 at TC-DSB (Fig. 4d, Extended Data Fig. 6l).

291 In agreement with our above findings, depletion of SUN1, NUP153 and RNF4 all impaired cell
292 survival post TC-DSB induction, while SUN2 did not, suggesting deficient repair upon
293 impairment of the TC-DSB NE-anchoring pathway (Fig. 4e-g). SUN1 and NUP153 depletion
294 also impaired cell survival following etoposide in RPE1 cells (Extended Data. Fig. 6m).
295 Importantly co-depletion of both SUN1 and PER1 or PER2 did not exacerbate the impaired
296 survival observed upon depletion of PER1 or PER2 proteins independently (Fig. 4h). Similarly,
297 co-depletion of NUP153 and PER2 or SUN1 did not trigger a significant decrease of cell
298 survival as compared to NUP153 depletion alone (Fig. 4i), nor did co-depletion of RNF4 and
299 PER2 (Fig. 4j), indicating they belong to the same pathway.

300 Taken together, our data suggest that TC-DSB anchoring to the NE mediated by a PER2, SUN1,
301 NUP153 and RNF4-dependent pathway, fosters RAD51 assembly, thereby ensuring efficient
302 repair and cell survival post DSB induction.

303

304 **PER2-mediated DSB anchoring to the NE counteracts DSB clustering and D-
305 compartment formation.**

306 In mammalian nuclei, principal component analysis (PCA) of Hi-C experiments revealed that
307 chromatin compartmentalizes to form the so-called “A” and “B” compartments, with the B-

308 compartment corresponding to microscopically visible heterochromatin foci, while the A-
309 compartment correspond to euchromatin⁵⁶. Of interest, both experimental data and
310 computational modeling of chromosome behaviour showed that targeting at the nuclear lamina
311 prevents heterochromatin to coalesce into internal larger nuclear bodies⁵⁷. The current model
312 postulates that upon detachment of chromatin from the NE, phase separation allows multiple
313 HC foci to cluster thus increasing B-compartmentalization. Importantly, we recently reported
314 that upon DSB induction, another chromatin compartment forms, so called the D-compartment
315 (for DSB-induced), through polymer-polymer phase separation¹¹. This D-compartment that
316 arises via DSB clustering gathers γH2AX-modified topologically associated domains (TADs)
317 as well as additional undamaged loci, including a subclass of DSB-activated genes¹¹.

318 Of interest, our siRNA screen indicated that the depletion of NONO, SETX and DDX17
319 increased clustering (Fig. 1b, Extended data Fig. 1f) and we found that PER2 contributes in
320 DSBs targeting to the NE (Fig. 3). Hence, we set out to investigate whether PER2 depletion
321 could also increase DSB clustering and D-compartment formation as a result of a lack of
322 damaged TADs anchoring at the NE. To address this point, we performed Hi-C experiments
323 before and after DSB induction in PER2-proficient and deficient cells. PER2 depletion did not
324 drastically affect chromosome organization in undamaged cells (Extended Data Fig. 7a), nor
325 the overall distribution of A and B compartments (Extended Data Fig. 7b). However, PER2
326 depletion triggered increased compartmentalization as visualized by increased A-A and B-B
327 interaction, as well as decreased A-B interaction (Extended Data Fig. 7c). This agrees with the
328 previously reported role of the PER complex in chromatin anchoring at the NE which would
329 predict an increased compartmentalization upon NE detachment in PER-depleted cells. Upon
330 DSB induction, we could recapitulate our previous finding showing DSB clustering (Extended
331 Data Fig. 7d, arrows). Importantly, PER2 depletion increased DSB clustering as shown on
332 individual events (Fig. 5a, Extended Data Fig. 7d), average aggregate peak analysis (APA) plots

333 of inter-chromosomal or intra-chromosomal DSB-DSB contacts centered on all 80 best-induced
334 DSBs (Fig. 5b, Extended Data Fig. 7e) and box plots quantifying the interactions between DSBs
335 (Fig. 5c). PER2 depletion also triggered enhanced clustering of endogenous DSB hotspots
336 (Extended Data Fig. 7f) and of etoposide-induced DSBs as measured using quantitative high
337 throughput microscopy (Extended data Fig. 7g).

338 We further computed Chromosomal Eigen Vectors (CEV) using the first PC of Principal
339 Component Analysis (PCA) on differential Hi-C matrices to identify the D-compartment as
340 previously described¹¹. As expected, we could recapitulate D-compartment formation upon
341 damage in DIVA cells transfected with a control siRNA (Extended Data Fig. 7h). PER2
342 deficiency did not alter D-compartment detection on chromosomes previously found to display
343 D-compartment (Extended Data Fig. 7h). However, we could observe D-compartment
344 formation on additional chromosomes upon PER2 depletion (Fig. 5d). Collectively our data
345 suggest that PER proteins prevent DSB clustering and D-compartment formation by fostering
346 the targeting of TC-DSBs to the nuclear lamina.

347 D-compartment formation fosters the DNA damage response, but it also comes at the expense
348 of increased translocation rate^{12,25,58}. In agreement with the above data involving PER2 in
349 counteracting D-compartment formation, increased translocation frequency was observed upon
350 depletion of the PER complex proteins (Fig. 2c). Similarly, and in line with their involvement
351 in TC-DSB tethering at NE (Extended data Fig. 6d, Fig. 3g, Extended data Fig. 6g), SUN1 and
352 NUP153 depletion increased translocation (Fig. 5e) suggesting enhanced DSB clustering in
353 SUN1 and NUP153 deficient cells. Of note, this was not the case when depleting SUN2, in
354 agreement with the absence of SUN2 recruitment at DSBs. Moreover, in agreement with the
355 previously reported role of Slx5/8 in the relocation of persistent DSBs and arrested forks in
356 yeast^{14,19,40,51}, as well as of HC breaks in drosophila¹⁵, RNF4 depletion also increased
357 translocation frequency (Fig. 5e), suggesting enhanced DSB clustering in absence of the STUbL

358 RNF4. Importantly co-depletion of both SUN1 and PER1 or PER2 did not further increased
359 translocation compared to SUN1 depletion alone (Fig. 5f). Similarly, co-depletion of NUP153
360 and PER2 or SUN1 did not trigger a significant increase in translocation frequency as compared
361 to NUP153 depletion alone (Fig. 5g), nor did co-depletion of RNF4 and PER2 (Fig. 5h). Taken
362 together, our data suggest that TC-DSB anchoring to the NE mediated by a PER2, SUN1,
363 NUP153 and RNF4-dependent pathway, counteracts DSB clustering and translocations in
364 human cells.

365

366 **The circadian clock regulates the response to TC-DSBs and their anchoring to the NE.**

367 Given that the PER complex is a core component of the circadian clock, we set out to investigate
368 whether the circadian clock could also regulate the response to TC-DSBs. As expected,
369 dexamethasone treatment synchronized the circadian clock in both U2OS and DIvA cells, as
370 assessed by the cycling expression of PER2, BMAL1 and CRY2 (Extended Data Fig. 8a-b).
371 We further monitored γ H2AX foci formation in different cell cycle phases, at different time
372 points after dexamethasone-mediated circadian clock synchronization by combining γ H2AX
373 staining and EdU labeling, using quantitative high throughput microscopy in DIvA cells. In line
374 with the results obtained with the depletion of PER2 by siRNA, our data indicate that γ H2AX
375 foci intensity was increased post-DSB induction during the low-PER2 circadian phase (Fig. 6a,
376 white bars; Extended Data Fig. 8c) as compared to the high-PER2 phase (Fig. 6a blue bars;
377 Extended Data Fig. 8c). This was independent of the cell cycle phase (Fig. 6a). Moreover,
378 increased accumulation of γ H2AX at TC-DSBs during the low-PER2 phase, was further
379 confirmed by ChIP (Fig. 6b). Of importance the same holds true in S and G2 phases when DSBs
380 were induced using etoposide (Extended Data Fig. 8d). To further reinforce the notion that the
381 low-PER2 phase of the circadian clock impacts TC-DSB repair, we performed circadian clock

382 synchronization and analyzed several outputs that were affected by the depletion of PER2. First,
383 the circadian clock did not alter transcriptional repression in *cis* to DSBs (Extended Data Fig.
384 8e) as expected from PER2 depletion data (Fig. 4a). Second, as found using PER2 depletion
385 (Fig. 3d), the low-PER2 circadian phase reduced the recruitment of LaminB1 (Fig. 6c) and
386 SUN1 (Fig. 6d) to TC-DSBs when monitored by ChIP-qPCR, suggesting that DSB anchoring
387 at the NE is defective when the PER1/2 proteins are expressed at low levels. Indeed,
388 γ H2AX/LaminB1 PLA signal decreased during the low PER2 phase (Fig. 6e). Third, given that
389 our data indicated a role of PER2 in RAD51 loading at TC-DSBs (Fig. 4c), we assessed RAD51
390 recruitment using ChIP. As expected from PER2 depletion data, RAD51 recruitment at TC-
391 DSBs decreased during the low PER phase (Fig. 6f). In agreement, RAD51 foci formation
392 monitored using high throughput microscopy at different time points after dexamethasone
393 treatment revealed an impaired RAD51 foci formation during the low-PER2 phase (Extended
394 Data Fig. 8f). Fourth, quantitative high throughput microscopy further showed an increase in
395 γ H2AX foci area during the low-PER2 phase, in agreement with enhanced DSB clustering (Fig.
396 6g).

397 We previously reported that, in addition to γ H2AX domains, the D-compartment also physically
398 attracts additional loci including some, but not all, DNA damage responsive (DDR) genes, in
399 order to potentiate their activation post-DSB induction²⁵. Notably, we found that *RNF19B* and
400 *PLK3*, two upregulated DDR genes found within the D-compartment, were significantly more
401 activated post-DSB during the low-PER2 phase when compared to the high-PER2 phase (Fig.
402 6h). This agrees with an increased D-compartment formation in absence of PER2 (Fig. 5a-d,
403 Extended Data Fig. 7h). Of importance, this was not the case for other DDR genes which are
404 not targeted to the D-compartment (*PPM1D*, *SLC9A1*)²⁵, or for other non-induced genes
405 (*LPHN2*, *UTP18*). Altogether these data indicate that the circadian rhythm regulates the repair

406 and signaling of TC-DSBs by controlling their PER2-dependent anchoring to the NE and,
407 therefore, the formation of the D-compartment, further fine-tuning the response to DSBs.

408

409 **Discussion**

410 In this study, we uncovered that the repair of DSBs occurring in transcriptionally active
411 chromatin in human requires their anchoring to the NE, a process that is under the direct control
412 of PERIOD proteins and is therefore sensitive to circadian oscillations (Fig. 6i). Notably, in a
413 recent preprint, the Mekhail lab reports that etoposide induces nuclear envelope tubules
414 (dsbNET) inside the nucleus which establish contacts with DSBs to foster repair⁵⁹. Since
415 persistent DSBs and arrested forks in yeast as well as HC breaks in *Drosophila*, also relocate
416 to the NE and NPC, altogether our findings suggest that targeting repair refractory DSBs to this
417 specific nuclear microenvironment is evolutionary conserved.

418 Of interest, previous work uncovered that the maintenance of genomic integrity and cancer
419 progression are tightly linked to the circadian clock⁶⁰⁻⁶². In general, genes involved in DNA
420 repair pathways are transcriptionally regulated by the circadian clock^{61,63-68}. Here we found that
421 in human cells, PER2 is directly targeted at DSBs. In contrast to a very recent report⁶⁹, we
422 observed neither BMAL1 binding at TC-DSBs, although BMAL1 distribution on the genome
423 behaved as expected, nor a function of BMAL1/CLOCK heterodimer in promoting cell survival
424 and counteracting translocation upon TC-DSBs induction in DIVA cells. This difference may
425 arise from analyzing overexpressed⁶⁹ versus endogenous (our study) BMAL1, from the DSB-
426 inducible systems used in both studies (AsiSI versus Zeocin and I-PpoI) and/or from difference
427 in the time points analyzed post-DSB induction.

428 Upon PER1 or PER2 depletion, as well as during the low-PER phase, γ H2AX level was
429 increased while RAD51 assembly was reduced suggesting a decreased repair capacity. Of

430 interest, in the accompanying paper, the Huertas lab reports that CRY1 is also recruited at
431 radiation-induced DSBs, where it directly represses resection and HR. Altogether our studies
432 suggest a two-arm control of HR repair during the 24h circadian cycle, with minimum HR
433 occurring at night in diurnal species. Indeed, large transcriptomic surveys, performed in
434 baboon⁶³ and very recently in human⁷⁰, allowed to carefully establish the transcriptional pattern
435 of core clock regulators during the day. PERIOD genes *Per1*, *Per2* and *Cry2* display a
436 maximum expression level around noon, while *Cry1* expression peaks at sunset, in agreement
437 with a PERIOD complex-independent function of CRY1. This allows us to propose the
438 following model (Extended Data Fig. 8g): in the morning, the presence of the PERIOD
439 PER1/PER2 proteins combined with the absence of CRY1, establishes an environment that
440 favors HR repair of TC-DSBs by allowing resection to occur, DSB anchoring to the NE and
441 RAD51 loading. Subsequently, the gradual increase of CRY1 during the afternoon causes
442 minimum resection at nightfall. The absence of PERIOD complex expression early at night
443 establishes a second layer of HR repression during the night. The gradual decrease of CRY1,
444 combined with the re-expression of PER proteins, then allows HR to resume the next morning.
445 Of interest, sleep was found to regulate the repair of physiological DSBs in neurons⁷¹, so
446 whether such a circadian regulation of TC-DSB repair also takes place in post-mitotic cells will
447 deserve further investigation.

448 In summary, our findings have implications for disease etiology and treatment. Indeed,
449 evidence suggests that a dysregulation of the circadian clock contributes to the progression of
450 neurodegenerative disorders⁷² and cancer initiation and progression^{60,62}, both types of diseases
451 being tightly coupled to DSB repair mechanisms and the maintenance of genome integrity.
452 Moreover, and importantly, topoisomerase II poison-based chemotherapies are a first-line
453 treatment against a number of cancers and given that these poisons mainly trigger DSBs in

454 active chromatin, our findings that circadian rhythm regulates the repair of TC-DSBs may be
455 an important feature to take into account for chronochemotherapy.

456

457 **Data and Code availability**

458 Code is available at <https://github.com/LegubeDNAREPAIR/CircadianClock>. High throughput
459 data are available at Array Express (E-MTAB-12712) using the link
460 <https://www.ebi.ac.uk/biostudies/arrayexpress/studies/E-MTAB-12712?key=2f8af589-d077-466a-a563-725b33761cda>

462

463 **Acknowledgments**

464 We thank the genomics core facility of EMBL for high-throughput sequencing. We thank
465 Vanessa Dougados for her help during the RIM acquisitions and the LITC TRI-GENOTOUL
466 photonic imaging platform. We thank L. Ligat from the CRCT Cell Imaging Platform
467 (INSERM-UMR1037) for technical assistance in high-content microscopy. We thank T.
468 Clouaire and N. Firmin for technical help. We thank T. Clouaire, and E. Cau for their advice
469 throughout the project and critical reading of the manuscript. Development of 3D RIM on the
470 LITC was supported by ANR-20-CE45-0024. Funding in GL laboratory was provided by grants
471 from the European Research Council (ERC-2014-CoG 647344; and ERC-AdG-101019963),
472 the Agence Nationale pour la Recherche (ANR-18-CE12-0015), the Fondation ARC pour la
473 recherche sur le cancer, the ITMO Cancer, the Ligue Nationale Contre le Cancer, comité de
474 l'Aude and the Fondation Bettencourt-Schueller. C.A was a recipient of a FRM fellowship
475 (FRM FDT201904007941), S.C. was a recipient of a PhD fellowship from Joint Training and
476 Research Programme on Chromatin Dynamics & the DNA Damage Response (H2020 ITN
477 aDDReSS, grant N° 812829), J.F is a recipient of a PhD fellowship from the Horizon Europe

478 Marie Skłodowska-Curie Actions Doctoral Networks CohesiNet (Grant Agreement No.
479 859853). I.L. is supported by a funding from the Fondation ARC pour la recherche sur le cancer.
480 N.P and P.C are INSERM researchers.

481

482 **Authors contributions**

483 B.L.B, L.G.S, J.F, R.C, E.G, C.P, C.A, I.L, A.G, A.L.F, A.M. and N.P, performed and analyzed
484 experiments. P.F and P.C optimized the mAID-AsiSIER lentiviral construct. S.C, M.A, and
485 V.R performed bioinformatic analyses of all high-throughput sequencing datasets. T.M
486 performed RIM acquisition and analysis. G.L. and N.P. supervised the work. G.L. wrote the
487 manuscript. All authors commented, edited and approved the manuscript.

488

489 **Conflict of interest**

490

491 The authors declare no competing interest

492

493 **References**

- 494 1. Marnef, A., Cohen, S., and Legube, G. (2017). Transcription-Coupled DNA Double-
495 Strand Break Repair: Active Genes Need Special Care. *Journal of Molecular Biology* 429,
496 1277–1288. 10.1016/j.jmb.2017.03.024.
- 497 2. Canela, A., Maman, Y., Huang, S.N., Wutz, G., Tang, W., Zagnoli-Vieira, G., Callen, E.,
498 Wong, N., Day, A., Peters, J.-M., et al. (2019). Topoisomerase II-Induced Chromosome
499 Breakage and Translocation Is Determined by Chromosome Architecture and
500 Transcriptional Activity. *Molecular Cell* 75, 252-266.e8. 10.1016/j.molcel.2019.04.030.
- 501 3. Ballarino, R., Bouwman, B.A.M., Agostini, F., Harbers, L., Diekmann, C., Wernersson,
502 E., Bienko, M., and Crosetto, N. (2022). An atlas of endogenous DNA double-strand
503 breaks arising during human neural cell fate determination. *Sci Data* 9, 400.
504 10.1038/s41597-022-01508-x.
- 505 4. Gothe, H.J., Bouwman, B.A.M., Gusmao, E.G., Piccinno, R., Petrosino, G., Sayols, S.,
506 Drechsel, O., Minneker, V., Josipovic, N., Mizi, A., et al. (2019). Spatial Chromosome
507 Folding and Active Transcription Drive DNA Fragility and Formation of Oncogenic MLL
508 Translocations. *Mol Cell* 75, 267-283.e12. 10.1016/j.molcel.2019.05.015.

509 5. Madabhushi, R., Gao, F., Pfenning, A.R., Pan, L., Yamakawa, S., Seo, J., Rueda, R.,
510 Phan, T.X., Yamakawa, H., Pao, P.-C., et al. (2015). Activity-Induced DNA Breaks
511 Govern the Expression of Neuronal Early-Response Genes. *Cell* *161*, 1592–1605.
512 10.1016/j.cell.2015.05.032.

513 6. Pankotai, T., Bonhomme, C., Chen, D., and Soutoglou, E. (2012). DNAPKcs-dependent
514 arrest of RNA polymerase II transcription in the presence of DNA breaks. *Nat Struct Mol*
515 *Biol* *19*, 276–282. 10.1038/nsmb.2224.

516 7. Shanbhag, N.M., Rafalska-Metcalf, I.U., Balane-Bolivar, C., Janicki, S.M., and
517 Greenberg, R.A. (2010). ATM-dependent chromatin changes silence transcription in cis
518 to DNA double-strand breaks. *Cell* *141*, 970–981. 10.1016/j.cell.2010.04.038.

519 8. Aymard, F., Bugler, B., Schmidt, C.K., Guillou, E., Caron, P., Briois, S., Iacovoni, J.S.,
520 Daburon, V., Miller, K.M., Jackson, S.P., et al. (2014). Transcriptionally active chromatin
521 recruits homologous recombination at DNA double-strand breaks. *Nat Struct Mol Biol* *21*,
522 366–374. 10.1038/nsmb.2796.

523 9. Ouyang, J., Yadav, T., Zhang, J.-M., Yang, H., Rheinbay, E., Guo, H., Haber, D.A., Lan,
524 L., and Zou, L. (2021). RNA transcripts stimulate homologous recombination by forming
525 DR-loops. *Nature* *594*, 283–288. 10.1038/s41586-021-03538-8.

526 10. Aymard, F., Aguirrebengoa, M., Guillou, E., Javierre, B.M., Bugler, B., Arnould, C.,
527 Rocher, V., Iacovoni, J.S., Biernacka, A., Skrzypczak, M., et al. (2017). Genome-wide
528 mapping of long-range contacts unveils clustering of DNA double-strand breaks at
529 damaged active genes. *Nat Struct Mol Biol* *24*, 353–361. 10.1038/nsmb.3387.

530 11. Arnould, C., Rocher, V., Saur, F., Bader, A.S., Muzzopappa, F., Collins, S., Lesage, E.,
531 Le Bozec, B., Puget, N., Clouaire, T., et al. (2023). Chromatin compartmentalization
532 regulates the response to DNA damage. *Nature* *623*, 183–192. 10.1038/s41586-023-
533 06635-y.

534 12. Zagelbaum, J., Schooley, A., Zhao, J., Schrank, B.R., Callen, E., Zha, S., Gottesman,
535 M.E., Nussenzweig, A., Rabidan, R., Dekker, J., et al. (2022). Multiscale reorganization
536 of the genome following DNA damage facilitates chromosome translocations via nuclear
537 actin polymerization. *Nat Struct Mol Biol*. 10.1038/s41594-022-00893-6.

538 13. Marnef, A., Finoux, A.-L., Arnould, C., Guillou, E., Daburon, V., Rocher, V., Mangeat,
539 T., Mangeot, P.E., Ricci, E.P., and Legube, G. (2019). A cohesin/HUSH- and LINC-
540 dependent pathway controls ribosomal DNA double-strand break repair. *Genes Dev.* *33*,
541 1175–1190. 10.1101/gad.324012.119.

542 14. Nagai, S., Dubrana, K., Tsai-Pflugfelder, M., Davidson, M.B., Roberts, T.M., Brown,
543 G.W., Varela, E., Hediger, F., Gasser, S.M., and Krogan, N.J. (2008). Functional
544 Targeting of DNA Damage to a Nuclear Pore-Associated SUMO-Dependent Ubiquitin
545 Ligase. *Science* *322*, 597–602. 10.1126/science.1162790.

546 15. Ryu, T., Spatola, B., Delabaere, L., Bowlin, K., Hopp, H., Kunitake, R., Karpen, G.H.,
547 and Chiolo, I. (2015). Heterochromatic breaks move to the nuclear periphery to continue
548 recombinational repair. *Nat Cell Biol* *17*, 1401–1411. 10.1038/ncb3258.

549 16. Oza, P., Jaspersen, S.L., Miele, A., Dekker, J., and Peterson, C.L. (2009). Mechanisms
550 that regulate localization of a DNA double-strand break to the nuclear periphery. *Genes*
551 *Dev.* *23*, 912–927. 10.1101/gad.1782209.

552 17. Horigome, C., Oma, Y., Konishi, T., Schmid, R., Marcomini, I., Hauer, M.H., Dion, V.,
553 Harata, M., and Gasser, S.M. (2014). SWR1 and INO80 Chromatin Remodelers
554 Contribute to DNA Double-Strand Break Perinuclear Anchorage Site Choice. *Molecular*
555 *Cell* *55*, 626–639. 10.1016/j.molcel.2014.06.027.

556 18. Kramarz, K., Schirmeisen, K., Boucherit, V., Ait Saada, A., Lovo, C., Palancade, B.,
557 Freudenreich, C., and Lambert, S.A.E. (2020). The nuclear pore primes recombination-
558 dependent DNA synthesis at arrested forks by promoting SUMO removal. *Nat Commun*
559 *11*, 5643. 10.1038/s41467-020-19516-z.

560 19. Whalen, J.M., Dhingra, N., Wei, L., Zhao, X., and Freudenreich, C.H. (2020). Relocation
561 of Collapsed Forks to the Nuclear Pore Complex Depends on Sumoylation of DNA
562 Repair Proteins and Permits Rad51 Association. *Cell Rep* *31*, 107635.
563 10.1016/j.celrep.2020.107635.

564 20. Iacovoni, J.S., Caron, P., Lassadi, I., Nicolas, E., Massip, L., Trouche, D., and Legube, G.
565 (2010). High-resolution profiling of γH2AX around DNA double strand breaks in the
566 mammalian genome. *EMBO J* *29*, 1446–1457. 10.1038/emboj.2010.38.

567 21. Crosetto, N., Mitra, A., Silva, M.J., Bienko, M., Dojer, N., Wang, Q., Karaca, E., Chiarle,
568 R., Skrzypczak, M., Ginalski, K., et al. (2013). Nucleotide-resolution DNA double-strand
569 break mapping by next-generation sequencing. *Nat Methods* *10*, 361–365.
570 10.1038/nmeth.2408.

571 22. Clouaire, T., Rocher, V., Lashgari, A., Arnould, C., Aguirrebengoa, M., Biernacka, A.,
572 Skrzypczak, M., Aymard, F., Fongang, B., Dojer, N., et al. (2018). Comprehensive
573 Mapping of Histone Modifications at DNA Double-Strand Breaks Deciphers Repair
574 Pathway Chromatin Signatures. *Molecular Cell* *72*, 250-262.e6.
575 10.1016/j.molcel.2018.08.020.

576 23. Cohen, S., Puget, N., Lin, Y.-L., Clouaire, T., Aguirrebengoa, M., Rocher, V., Pasero, P.,
577 Canitrot, Y., and Legube, G. (2018). Senataxin resolves RNA:DNA hybrids forming at
578 DNA double-strand breaks to prevent translocations. *Nat Commun* *9*, 533.
579 10.1038/s41467-018-02894-w.

580 24. Cohen, S., Guenolé, A., Lazar, I., Marnef, A., Clouaire, T., Vernekar, D.V., Puget, N.,
581 Rocher, V., Arnould, C., Aguirrebengoa, M., et al. (2022). A POLD3/BLM dependent
582 pathway handles DSBs in transcribed chromatin upon excessive RNA:DNA hybrid
583 accumulation. *Nat Commun* *13*, 2012. 10.1038/s41467-022-29629-2.

584 25. Arnould, C., Rocher, V., Bader, A.S., Lesage, E., Puget, N., Clouaire, T., Mourad, R.,
585 Noordermeer, D., Bushell, M., and Legube, G. (2021). ATM-dependent formation of a
586 novel chromatin compartment regulates the Response to DNA Double Strand Breaks and
587 the biogenesis of translocations (Molecular Biology) 10.1101/2021.11.07.467654.

588 26. Brown, S.A., Ripperger, J., Kadener, S., Fleury-Olela, F., Vilbois, F., Rosbash, M., and
589 Schibler, U. (2005). PERIOD1-Associated Proteins Modulate the Negative Limb of the
590 Mammalian Circadian Oscillator. *Science* *308*, 693–696. 10.1126/science.1107373.

591 27. Duong, H.A., Robles, M.S., Knutti, D., and Weitz, C.J. (2011). A Molecular Mechanism
592 for Circadian Clock Negative Feedback. *Science* *332*, 1436–1439.
593 10.1126/science.1196766.

594 28. Padmanabhan, K., Robles, M.S., Westerling, T., and Weitz, C.J. (2012). Feedback
595 Regulation of Transcriptional Termination by the Mammalian Circadian Clock PERIOD
596 Complex. *Science* *337*, 599–602. 10.1126/science.1221592.

597 29. Kim, J.Y., Kwak, P.B., and Weitz, C.J. (2014). Specificity in Circadian Clock Feedback
598 from Targeted Reconstitution of the NuRD Corepressor. *Molecular Cell* *56*, 738–748.
599 10.1016/j.molcel.2014.10.017.

600 30. Emerson, J.M., Bartholomai, B.M., Ringelberg, C.S., Baker, S.E., Loros, J.J., and Dunlap,
601 J.C. (2015). *period* -1 encodes an ATP-dependent RNA helicase that influences
602 nutritional compensation of the *Neurospora* circadian clock. *Proc. Natl. Acad. Sci. U.S.A.*
603 *112*, 15707–15712. 10.1073/pnas.1521918112.

604 31. Ogilvie, V.C. (2003). The highly related DEAD box RNA helicases p68 and p72 exist as
605 heterodimers in cells. *Nucleic Acids Research* *31*, 1470–1480. 10.1093/nar/gkg236.

606 32. Takahashi, J.S. (2017). Transcriptional architecture of the mammalian circadian clock.
607 *Nat Rev Genet* *18*, 164–179. 10.1038/nrg.2016.150.

608 33. Sessa, G., Gómez-González, B., Silva, S., Pérez-Calero, C., Beaurepere, R., Barroso, S.,
609 Martineau, S., Martin, C., Ehlén, Å., Martínez, J.S., et al. (2021). BRCA2 promotes
610 DNA-RNA hybrid resolution by DDX5 helicase at DNA breaks to facilitate their repair‡.
611 *EMBO J* *40*, e106018. 10.15252/embj.2020106018.

612 34. Qu, M., Qu, H., Jia, Z., and Kay, S.A. (2021). HNF4A defines tissue-specific circadian
613 rhythms by beaconing BMAL1::CLOCK chromatin binding and shaping the rhythmic
614 chromatin landscape. *Nat Commun* *12*, 6350. 10.1038/s41467-021-26567-3.

615 35. Koike, N., Yoo, S.-H., Huang, H.-C., Kumar, V., Lee, C., Kim, T.-K., and Takahashi, J.S.
616 (2012). Transcriptional Architecture and Chromatin Landscape of the Core Circadian
617 Clock in Mammals. *Science* *338*, 349–354. 10.1126/science.1226339.

618 36. Tartour, K., and Padmanabhan, K. (2022). The Clock Takes Shape—24 h Dynamics in
619 Genome Topology. *Front. Cell Dev. Biol.* *9*, 799971. 10.3389/fcell.2021.799971.

620 37. Xiao, Y., Yuan, Y., Jimenez, M., Soni, N., and Yadlapalli, S. (2021). Clock proteins
621 regulate spatiotemporal organization of clock genes to control circadian rhythms. *Proc.*
622 *Natl. Acad. Sci. U.S.A.* *118*, e2019756118. 10.1073/pnas.2019756118.

623 38. Kalocsay, M., Hiller, N.J., and Jentsch, S. (2009). Chromosome-wide Rad51 Spreading
624 and SUMO-H2A.Z-Dependent Chromosome Fixation in Response to a Persistent DNA
625 Double-Strand Break. *Molecular Cell* *33*, 335–343. 10.1016/j.molcel.2009.01.016.

626 39. Horigome, C., Unozawa, E., Ooki, T., and Kobayashi, T. (2019). Ribosomal RNA gene
627 repeats associate with the nuclear pore complex for maintenance after DNA damage.
628 *PLoS Genet* 15, e1008103. 10.1371/journal.pgen.1008103.

629 40. Horigome, C., Bustard, D.E., Marcomini, I., Delgoshai, N., Tsai-Pflugfelder, M., Cobb,
630 J.A., and Gasser, S.M. (2016). PolySUMOylation by Siz2 and Mms21 triggers relocation
631 of DNA breaks to nuclear pores through the Slx5/Slx8 STUbL. *Genes Dev.* 30, 931–945.
632 10.1101/gad.277665.116.

633 41. Oshidari, R., Strecker, J., Chung, D.K.C., Abraham, K.J., Chan, J.N.Y., Damaren, C.J.,
634 and Mekhail, K. (2018). Nuclear microtubule filaments mediate non-linear directional
635 motion of chromatin and promote DNA repair. *Nat Commun* 9, 2567. 10.1038/s41467-
636 018-05009-7.

637 42. Chung, D.K.C., Chan, J.N.Y., Strecker, J., Zhang, W., Ebrahimi-Ardebili, S., Lu, T.,
638 Abraham, K.J., Durocher, D., and Mekhail, K. (2015). Perinuclear tethers license
639 telomeric DSBs for a broad kinesin- and NPC-dependent DNA repair process. *Nat
640 Commun* 6, 7742. 10.1038/ncomms8742.

641 43. Khadaroo, B., Teixeira, M.T., Luciano, P., Eckert-Boulet, N., Germann, S.M., Simon,
642 M.N., Gallina, I., Abdallah, P., Gilson, E., Géli, V., et al. (2009). The DNA damage
643 response at eroded telomeres and tethering to the nuclear pore complex. *Nat Cell Biol* 11,
644 980–987. 10.1038/ncb1910.

645 44. Pinzaru, A.M., Kareh, M., Lamm, N., Lazzerini-Denchi, E., Cesare, A.J., and Sfeir, A.
646 (2020). Replication stress conferred by POT1 dysfunction promotes telomere
647 relocalization to the nuclear pore. *Genes Dev* 34, 1619–1636. 10.1101/gad.337287.120.

648 45. Lamm, N., Read, M.N., Nobis, M., Van Ly, D., Page, S.G., Masamsetti, V.P., Timpson,
649 P., Biro, M., and Cesare, A.J. (2020). Nuclear F-actin counteracts nuclear deformation
650 and promotes fork repair during replication stress. *Nat Cell Biol* 22, 1460–1470.
651 10.1038/s41556-020-00605-6.

652 46. Caridi, C.P., D'Agostino, C., Ryu, T., Zapotoczny, G., Delabaere, L., Li, X.,
653 Khodaverdian, V.Y., Amaral, N., Lin, E., Rau, A.R., et al. (2018). Nuclear F-actin and
654 myosins drive relocalization of heterochromatic breaks. *Nature* 559, 54–60.
655 10.1038/s41586-018-0242-8.

656 47. Mangeat, T., Labouesse, S., Allain, M., Negash, A., Martin, E., Guénolé, A., Poincloux,
657 R., Estibal, C., Bouissou, A., Cantaloube, S., et al. (2021). Super-resolved live-cell
658 imaging using random illumination microscopy. *Cell Reports Methods* 1, 100009.
659 10.1016/j.crmeth.2021.100009.

660 48. Lottersberger, F., Karssemeijer, R.A., Dimitrova, N., and de Lange, T. (2015). 53BP1 and
661 the LINC Complex Promote Microtubule-Dependent DSB Mobility and DNA Repair.
662 *Cell* 163, 880–893. 10.1016/j.cell.2015.09.057.

663 49. Liu, Q., Pante, N., Misteli, T., Elsagga, M., Crisp, M., Hodzic, D., Burke, B., and Roux,
664 K.J. (2007). Functional association of Sun1 with nuclear pore complexes. *Journal of Cell
665 Biology* 178, 785–798. 10.1083/jcb.200704108.

666 50. Li, P., and Noegel, A.A. (2015). Inner nuclear envelope protein SUN1 plays a prominent
667 role in mammalian mRNA export. *Nucleic Acids Res*, gkv1058. 10.1093/nar/gkv1058.

668 51. Su, X.A., Dion, V., Gasser, S.M., and Freudenreich, C.H. (2015). Regulation of
669 recombination at yeast nuclear pores controls repair and triplet repeat stability. *Genes Dev*
670 29, 1006–1017. 10.1101/gad.256404.114.

671 52. Caron, P., van der Linden, J., and van Attikum, H. (2019). Bon voyage: A transcriptional
672 journey around DNA breaks. *DNA Repair* 82, 102686. 10.1016/j.dnarep.2019.102686.

673 53. Zhou, Y., Caron, P., Legube, G., and Paull, T.T. (2014). Quantitation of DNA double-
674 strand break resection intermediates in human cells. *Nucleic Acids Research* 42, e19–e19.
675 10.1093/nar/gkt1309.

676 54. Galanty, Y., Belotserkovskaya, R., Coates, J., and Jackson, S.P. (2012). RNF4, a SUMO-
677 targeted ubiquitin E3 ligase, promotes DNA double-strand break repair. *Genes Dev* 26,
678 1179–1195. 10.1101/gad.188284.112.

679 55. Han, M.M., Hirakawa, M., Yamauchi, M., and Matsuda, N. (2022). Roles of the SUMO-
680 related enzymes, PIAS1, PIAS4, and RNF4, in DNA double-strand break repair by
681 homologous recombination. *Biochem Biophys Res Commun* 591, 95–101.
682 10.1016/j.bbrc.2021.12.099.

683 56. Lieberman-Aiden, E., van Berkum, N.L., Williams, L., Imakaev, M., Ragoczy, T.,
684 Telling, A., Amit, I., Lajoie, B.R., Sabo, P.J., Dorschner, M.O., et al. (2009).
685 Comprehensive Mapping of Long-Range Interactions Reveals Folding Principles of the
686 Human Genome. *Science* 326, 289–293. 10.1126/science.1181369.

687 57. Falk, M., Feodorova, Y., Naumova, N., Imakaev, M., Lajoie, B.R., Leonhardt, H., Joffe,
688 B., Dekker, J., Fudenberg, G., Solovei, I., et al. (2019). Heterochromatin drives
689 compartmentalization of inverted and conventional nuclei. *Nature* 570, 395–399.
690 10.1038/s41586-019-1275-3.

691 58. Roukos, V., Voss, T.C., Schmidt, C.K., Lee, S., Wangsa, D., and Misteli, T. (2013).
692 Spatial Dynamics of Chromosome Translocations in Living Cells. *Science* 341, 660–664.
693 10.1126/science.1237150.

694 59. Shokrollahi, M., Stanic, M., Hundal, A., Chan, J. N.Y., Urman, D., Hakem, A., Garcia,
695 R.E., Hao, J., Maass, P.G., Dickson, B.C., et al. (2023). DNA double-strand break-
696 capturing nuclear envelope tubules drive DNA repair. *bioRxiv*, 2023.05.07.539750.
697 10.1101/2023.05.07.539750.

698 60. Sancar, A., and Van Gelder, R.N. (2021). Clocks, cancer, and chronochemotherapy.
699 *Science* 371, eabb0738. 10.1126/science.abb0738.

700 61. Kondratov, R.V., and Antoch, M.P. (2007). Circadian proteins in the regulation of cell
701 cycle and genotoxic stress responses. *Trends in Cell Biology* 17, 311–317.
702 10.1016/j.tcb.2007.07.001.

703 62. Masri, S., and Sassone-Corsi, P. (2018). The emerging link between cancer, metabolism,
704 and circadian rhythms. *Nat Med* 24, 1795–1803. 10.1038/s41591-018-0271-8.

705 63. Mure, L.S., Le, H.D., Benegiamo, G., Chang, M.W., Rios, L., Jillani, N., Ngotho, M.,
706 Kariuki, T., Dkhissi-Benyahya, O., Cooper, H.M., et al. (2018). Diurnal transcriptome
707 atlas of a primate across major neural and peripheral tissues. *Science* *359*, eaao0318.
708 10.1126/science.aao0318.

709 64. Alexandrou, A.T., Duan, Y., Xu, S., Tepper, C., Fan, M., Tang, J., Berg, J., Basheer, W.,
710 Valicenti, T., Wilson, P.F., et al. (2022). PERIOD 2 regulates low-dose radioprotection
711 via PER2/pGSK3 β / β -catenin/Per2 loop. *iScience* *25*, 105546. 10.1016/j.isci.2022.105546.

712 65. Papp, S.J., Huber, A.-L., Jordan, S.D., Kriebs, A., Nguyen, M., Moresco, J.J., Yates, J.R.,
713 and Lamia, K.A. (2015). DNA damage shifts circadian clock time via HauSp-dependent
714 Cry1 stabilization. *eLife* *4*, e04883. 10.7554/eLife.04883.

715 66. Shafi, A.A., McNair, C.M., McCann, J.J., Alshalalfa, M., Shostak, A., Severson, T.M.,
716 Zhu, Y., Bergman, A., Gordon, N., Mandigo, A.C., et al. (2021). The circadian
717 cryptochrome, CRY1, is a pro-tumorigenic factor that rhythmically modulates DNA
718 repair. *Nat Commun* *12*, 401. 10.1038/s41467-020-20513-5.

719 67. Anabtawi, N., Cvammen, W., and Kemp, M.G. (2021). Pharmacological inhibition of
720 cryptochrome and REV-ERB promotes DNA repair and cell cycle arrest in cisplatin-
721 treated human cells. *Sci Rep* *11*, 17997. 10.1038/s41598-021-97603-x.

722 68. Gaddameedhi, S., Selby, C.P., Kaufmann, W.K., Smart, R.C., and Sancar, A. (2011).
723 Control of skin cancer by the circadian rhythm. *Proc. Natl. Acad. Sci. U.S.A.* *108*, 18790–
724 18795. 10.1073/pnas.1115249108.

725 69. Zhang, C., Chen, L., Sun, L., Jin, H., Ren, K., Liu, S., Qian, Y., Li, S., Li, F., Zhu, C., et
726 al. (2023). BMAL1 collaborates with CLOCK to directly promote DNA double-strand
727 break repair and tumor chemoresistance. *Oncogene*. 10.1038/s41388-023-02603-y.

728 70. Talamanca, L., Gobet, C., and Naef, F. (2023). Sex-dimorphic and age-dependent
729 organization of 24-hour gene expression rhythms in humans. *Science* *379*, 478–483.
730 10.1126/science.add0846.

731 71. Zada, D., Sela, Y., Matosevich, N., Monsonego, A., Lerer-Goldshtein, T., Nir, Y., and
732 Appelbaum, L. (2021). Parp1 promotes sleep, which enhances DNA repair in neurons.
733 *Molecular Cell* *81*, 4979-4993.e7. 10.1016/j.molcel.2021.10.026.

734 72. Nassan, M., and Videncovic, A. (2022). Circadian rhythms in neurodegenerative disorders.
735 *Nat Rev Neurol* *18*, 7–24. 10.1038/s41582-021-00577-7.

736 73. Caron, P., Choudjaye, J., Clouaire, T., Bugler, B., Daburon, V., Aguirrebengoa, M.,
737 Mangeat, T., Iacovoni, J.S., Álvarez-Quilón, A., Cortés-Ledesma, F., et al. (2015). Non-
738 redundant Functions of ATM and DNA-PKcs in Response to DNA Double-Strand
739 Breaks. *Cell Reports* *13*, 1598–1609. 10.1016/j.celrep.2015.10.024.

740 74. Natsume, T., Kiyomitsu, T., Saga, Y., and Kanemaki, M.T. (2016). Rapid Protein
741 Depletion in Human Cells by Auxin-Inducible Degron Tagging with Short Homology
742 Donors. *Cell Rep* *15*, 210–218. 10.1016/j.celrep.2016.03.001.

743 75. Nemoz, C., Ropars, V., Frit, P., Gontier, A., Drevet, P., Yu, J., Guerois, R., Pitois, A.,
744 Comte, A., Delteil, C., et al. (2018). XLF and APLF bind Ku80 at two remote sites to

745 ensure DNA repair by non-homologous end joining. *Nat Struct Mol Biol* 25, 971–980.
746 10.1038/s41594-018-0133-6.

747 76. Fu, C., Donovan, W.P., Shikapwashya-Hasser, O., Ye, X., and Cole, R.H. (2014). Hot
748 Fusion: an efficient method to clone multiple DNA fragments as well as inverted repeats
749 without ligase. *PLoS One* 9, e115318. 10.1371/journal.pone.0115318.

750 77. Cheng, Q., Barboule, N., Frit, P., Gomez, D., Bombarde, O., Couderc, B., Ren, G.-S.,
751 Salles, B., and Calsou, P. (2011). Ku counteracts mobilization of PARP1 and MRN in
752 chromatin damaged with DNA double-strand breaks. *Nucleic Acids Res* 39, 9605–9619.
753 10.1093/nar/gkr656.

754 78. Li, Q. (2004). A Syntaxin 1, G o, and N-Type Calcium Channel Complex at a Presynaptic
755 Nerve Terminal: Analysis by Quantitative Immunocolocalization. *Journal of*
756 *Neuroscience* 24, 4070–4081. 10.1523/JNEUROSCI.0346-04.2004.

757 79. van Steensel, B., van Binnendijk, E.P., Hornsby, C.D., van der Voort, H.T., Krozowski,
758 Z.S., de Kloet, E.R., and van Driel, R. (1996). Partial colocalization of glucocorticoid and
759 mineralocorticoid receptors in discrete compartments in nuclei of rat hippocampus
760 neurons. *Journal of Cell Science* 109, 787–792. 10.1242/jcs.109.4.787.

761 80. Arnould, C., Rocher, V., Finoux, A.-L., Clouaire, T., Li, K., Zhou, F., Caron, P.,
762 Mangeot, Philippe.E., Ricci, E.P., Mourad, R., et al. (2021). Loop extrusion as a
763 mechanism for formation of DNA damage repair foci. *Nature* 590, 660–665.
764 10.1038/s41586-021-03193-z.

765

766 **Figure Legends**

767

768 **Figure 1: A multi-output screen for the identification of new TC-DSBR factors.**

769 **a.** Experimental scheme: DIvA cells allow to temporally induce, following treatment with 4-
770 hydroxytamoxifen (4-OHT), DSBs at annotated positions on the human genome, among which
771 >50% fall in active loci (TC-DSBs). TC-DSB potential interacting partners were identified
772 through a proteomic approach¹³. 130 proteins were further subjected to a multi-output screen in
773 AID-DIvA cells using a siRNA library, to score DSB-induced γ H2AX foci intensity (using
774 quantitative high throughput imaging), DSB clustering (γ H2AX foci mean area), chromosome
775 rearrangement (illegitimate rejoining between two TC-DSBs *t(MIS12;TRIM37)* analyzed by
776 qPCR following DSB induction and repair) and cell survival (quantified eight days after DSB
777 induction, using a colorimetric assay based on mitochondrial dehydrogenase activity in viable
778 cells).

779 **b.** Heatmap of the z-score for the 4 outputs measured (γ H2AX foci intensity, Clustering,
780 Translocation and Survival) in the screen of the 130 genes of interest ordered by hierarchical
781 clustering (Pearson correlation distance/ward.D method) after normalization of the data to a
782 control siRNA (see Extended Data Fig. 1b-e). A positive control (SETX) was included in the
783 experiment (red). PPHLN1 and PER complex siRNAs are highlighted in green and blue
784 respectively.

785 **c.** Violin plots of scored outputs for the two groups of genes defined by the hierarchical
786 clustering. *P*, student t-test.

787 **d-g.** Scatter plots showing the correlations for each siRNA between γ H2AX intensity and cell
788 survival (**d**); γ H2AX intensity and translocations (**e**); translocations and DSB clustering (**f**) and

789 cell survival and translocations (g). The 95% confidence intervals and the coefficient of
790 correlation (r, Pearson) are indicated.

791

792 **Figure 2. PER proteins are recruited at TC-DSBs and regulate γ H2AX foci formation,
793 translocation, and cell survival upon DSB induction**

794 **a.** γ H2AX staining performed in control (CTRL), PER1 or PER2-siRNA transfected DIvA
795 cells, before (-DSB) and after (+DSB) DSB induction. Quantification (normalized against
796 Hoechst intensity) is shown on the bottom panel (>7000 nuclei, from a representative
797 experiment). Center line: median; box limits: 1st and 3rd quartiles; whiskers: maximum and
798 minimum without outliers. *P*, unpaired t-test.

799 **b.** γ H2AX ChIP performed in DIvA cells transfected with siRNA control (CTRL) or PER2
800 before and after DSB induction and analyzed by qPCR at two DSBs (DSB1-2). Data are
801 normalized to a control location devoid of a DSB. Mean and SEM are shown for n=4 biological
802 replicates. *P*, paired t-test (two-sided).

803 **c.** *t(MIS12:TRIM37)* rejoining frequencies after DSB induction measured by qPCR in AID-
804 DIvA cells transfected with siRNA CTRL, PER1 PER2, DDX17, SETX, NONO, DDX5 and
805 BMAL1. Mean and SD (n \geq 4 biological replicates) are shown. *P*, paired t-test (two-sided).

806 **d.** Clonogenic assays in AID-DIvA cells transfected with siRNA CTRL, PER1, PER2, DDX17,
807 NONO, DDX5 or BMAL1. Upper and lower panels show the mean and SEM after 4-OHT
808 treatment (+DSB) and after IAA treatment (+DSB+Repair) respectively (n \geq 4 biological
809 replicates). *P*, paired t-test (two-sided).

810 **e.** PER2, DDX5, DDX17 and BMAL1 ChIP efficiency (expressed as % of input
811 immunoprecipitated) before (-DSB) and after (+DSB) DSB induction, at a control genomic

812 locus devoid of DSB, a promoter (*BTG2* or *PER1* as indicated), and DSB1 or DSB4. Mean and
813 SEM are shown for $n \geq 10$ replicates. P , paired t-test (two-sided).

814 **f.** Genomic tracks showing RNA Polymerase II before DSB induction (RNAPII, green), BLESS
815 after DSB induction (black), as well as BMAL1 (blue) and PER2 (violet) ($\log_2(+\text{DSB}/-\text{DSB})$)
816 at a TC-DSB (upper panel; chr21:460221789) and a DSB induced in a silent locus (lower panel;
817 chr12:130091880). DSBs are indicated by arrows.

818 **g.** Average PER2 (left) and BMAL1 (right) ChIP-seq profiles on a ± 5 kb window centered on
819 the eighty best-induced AsiSI-DSBs (top) or eighty random sites (bottom, no DSB). Data are
820 presented in $\log_2(+\text{DSB}/-\text{DSB})$.

821 **h.** Box plots representing Log2 (+DSB/-DSB) PER2 ChIP-seq count on a ± 2 kb at HR-DSB,
822 NHEJ-DSB ($n=30$ in each category, among the 80 best-induced DSBs) or random sites ($n=30$).
823 Center line: median; box limits: 1st and 3rd quartiles; whiskers: maximum and minimum
824 without outliers. P , Wilcoxon test.

825

826 **Figure 3: TC-DSBs are targeted to the nuclear envelope via a PER2-dependent
827 mechanism**

828 **a.** Super-resolution live imaging performed using Random Illumination microscopy (RIM) in
829 DIvA cells expressing 53BP1-GFP and mCherry-LaminB1, starting >1 h after DSB induction.
830 Arrows show the establishment of a contact between a focus and nuclear lamina. Images were
831 acquired every 40 s.

832 **b.** Proximity Ligation Assay (PLA) performed using either 53BP1 antibody (top panels), Lamin
833 B1 antibody (middle panels) or both 53BP1 and LaminB1 antibodies (bottom panels) before (-
834 DSB) and after DSB (+DSB) induction in DIvA cells. PLA quantification is shown on the right

835 panel. An average of 190 cells were analyzed per condition. Center line: median; box limits:
836 1st and 3rd quartiles; whiskers: maximum and minimum without outliers. P , Wilcoxon test.

837 **c.** LaminB1 ChIP-qPCR before (−DSB) and after (+DSB) DSB induction, at TC-DSBs (HR-
838 DSBs, DSB1-4) and one DSB induced in a silent locus and repaired by NHEJ (DSB5). Data
839 are normalized to a control location devoid of a DSB. Mean and SEM are shown for n=7
840 biological replicates. P , paired t-test (two-sided).

841 **d.** LaminB1 ChIP-qPCR before (−DSB) and after (+DSB) DSB induction in control and PER2
842 siRNA-depleted DIVA cells, at TC-DSBs (DSB1-4, HR-DSBs) and a DSB in a silent locus
843 (DSB5, NHEJ-DSBs). Data are normalized to a control location devoid of DSB. Mean and
844 SEM are shown for n=4 biological replicates. P , paired t-test (two-sided).

845 **e.** Number of PLA foci (53BP1-LaminB1) in CTRL, PER1 or PER2-siRNA transfected DIVA
846 cells as indicated, before (−DSB) and after (+DSB) DSB induction. Data were normalized to
847 the untreated samples. Mean and SEM (n=3 biological replicates) are shown. P , paired t-test
848 (two-sided).

849 **f.** Genomic tracks of SUN1(purple) and SUN2 (dark blue) ChIP-seq ($\log_2(+\text{DSB}/-\text{DSB})$) at a
850 TC-DSB (upper panel; chr17:57184296) and a DSB induced in a silent locus (lower panel;
851 chr12:130091880).

852 **g.** Average profiles of SUN1 (left) and SUN2 (right) on a ± 5 kb window centered on the eighty
853 best-induced AsiSI-DSBs (top) or eighty random sites (bottom, no DSB). Data are presented as
854 $\log_2(+\text{DSB}/-\text{DSB})$.

855 **h.** Magnifications of SUN2 (top panels) and SUN1 (bottom panels) staining in nuclear envelope
856 (dotted line) together with γ H2AX foci in DIVA cells after DSB induction. Arrows indicate sites
857 of colocalization.

858 **i.** Cross Correlation Function (CCF) plots between γ H2AX foci and NE-embedded SUN2 (top
859 panel, N=70 γ H2AX foci) or SUN1 (bottom panel, N=46 γ H2AX foci). CCF of bicolor 3D RIM
860 images was determined by plotting the value of Pearson's correlation coefficient P[0.1] against
861 Δx for each voxel of the image (see methods). The arrows show a non-random exclusion
862 between γ H2AX and SUN2 (dip at $\Delta x=0$) or a non-random overlap between the signals of
863 SUN1 and γ H2AX (peak at $\Delta x=0$).

864 **j.** LaminB1 ChIP-qPCR before (−DSB) and after (+DSB) DSB induction in control and SUN1
865 siRNA-depleted DIvA cells, at two TC-DSBs (DSB1 and DSB3, HR-DSBs) and two DSBs in
866 silent loci (DSB5 and DSB6, NHEJ-DSBs). Data are normalized to a control location devoid
867 of DSB. Mean and SEM are shown for n=3 biological replicates. *P*, paired t-test (two-sided).

868 **k.** Left panel: Magnification of NUP153 staining in nuclear envelope (dotted line) together with
869 γ H2AX foci in DIvA cells after DSB induction. Arrows indicate sites of colocalization. Right
870 panel: CCF plot as above between γ H2AX foci and NPC protein NUP153 (N=28 γ H2AX foci)
871 showing a non-random overlap between both signals (peak at $\Delta x=0$).

872

873 **Figure 4. PER2 and SUN1-dependent anchoring at the Nuclear Pore Complex promotes
874 Homologous Recombination repair**

875 **a.** RT-qPCR performed before (−DSB) and after (+DSB) DSB induction in control (CTRL),
876 PER1 or PER2 siRNA-depleted DIvA cells for six genes carrying a TC-DSB (relative to
877 untreated sample (-DSB)). Mean and SEM are shown for n=6 biological replicates. *P*, paired t-
878 test (two-sided).

879 **b.** RT-qPCR performed before (−DSB) and after (+DSB) DSB induction in control (CTRL) or
880 SUN1 siRNA-depleted DIvA cells for six genes carrying a TC-DSB (relative to untreated

881 sample (-DSB)). Mean and SEM are shown for n=3 biological replicates. *P*, paired t-test (two-
882 sided).

883 **c.** RAD51 ChIP-qPCR in DIvA cells transfected with control or PER2 siRNA before and after
884 DSB induction, at four TC-DSBs (DSB1-4) and one DSB in a silent locus (DSB5). Data are
885 normalized to a control location devoid of a DSB, and further expressed relative to data obtained
886 at DSB4. Mean and SEM are shown for n=3 biological replicates. *P*, paired t-test (two-sided).

887 **d.** Ratios of RAD51 over RPA ChIP-qPCR results in DIvA cells transfected with control
888 (CTRL) or SUN1 siRNA after DSB induction, at four TC-DSBs (DSB1-4). Data are normalized
889 to a control location devoid of a DSB, and further expressed relative to data obtained at DSB4.
890 Mean and SEM are shown for n=3 biological replicates. *P*, paired t-test (two-sided).

891 **e-j.** Clonogenic assays in AID-DIvA cells transfected with the indicated siRNAs. Mean and
892 SEM of n biologically independent experiments after OHT and IAA treatment (DSB induction
893 and repair) are shown. *P*, paired t-test (two-sided). **e.** Control (CTRL), SUN1 or SUN2 siRNAs
894 (n=5). **f.** CTRL or NUP153 siRNAs (n=6). **g.** CTRL or RNF4 siRNAs (n=6). **h.** CTRL, PER1,
895 PER2, and double PER1+SUN1 and PER2+SUN1 siRNAs (n=4). **i.** CTRL, NUP153, and
896 double PER2+NUP153 and SUN1+NUP153 siRNAs (n=3). **j.** CTRL, PER2, RNF4 and double
897 PER2+RNF4 siRNAs (n=3).

898

899 **Figure 5. PER proteins, SUN1, NUP153 and RNF4-mediated TC-DSB anchoring to the**
900 **nuclear envelope counteract DSB clustering and D-compartment formation**

901 **a.** Differential Hi-C contact matrix [(+DSB)-(-DSB)] on a region located on chromosome 2 at
902 25kb resolution in DIvA cells transfected with a control siRNA or a siRNA directed against
903 PER2 as indicated. γ H2AX ChIP-seq track (+DSB) are also shown (dark red).

904 **b.** Interchromosomal DSB interaction shown as aggregate peak analysis (APA) plotted on a
905 200kb window (10kb resolution) before (-DSB) and after DSB (+DSB) induction in control and
906 PER2 siRNA-transfected DIvA cells for the eighty best-induced AsiSI-DSBs (left) or eighty
907 random sites (right, no DSB). FC: Fold change calculated between the central pixel and a square
908 of 3x3 pixels on the bottom left corner of the matrix. APAs show an increased signal at the
909 center (DSB-DSB interaction) after DSBs induction only for DSB sites (FC= 3.49, compared
910 to 0.89 for random sites)). The signal increases after PER2 depletion (FC= 3.85).

911 **c.** Box plot showing the differential Hi-C read counts (as (log2 +DSB/-DSB)) between the 80
912 best induced DSBs (+/- 500kb) (left) or 80 random sites (right) in control (CTRL, grey) and
913 PER2 (purple) siRNA-transfected DIvA cells. Center line: median; box limits: 1st and 3rd
914 quartiles; whiskers: maximum and minimum without outliers. *P*, non-parametric Wilcoxon test.

915 **d.** Genomic tracks of γ H2AX ChIP-seq after DSB induction (dark red) and of Chromosomal
916 Eigen vectors (CEV) obtained from PCA analyses performed on differential +DSB/-DSB Hi-
917 C matrices. CEV in siCTRL (grey) and siPER2 (blue). The D-compartment is represented as
918 positive values. siPER2 triggered the appearance of the D-compartment on the chromosome 2
919 normally devoid of D compartmentalization post-DSB induction in DIvA cells (areas
920 highlighted in light grey).

921 **e-h.** *t(MIS12:TRIM37)* rejoining frequency after DSB induction and repair measured by qPCR
922 in AID-DIvA cells transfected with the indicated siRNAs. Mean and SEM of n biological
923 replicates are shown. *P*, paired t-test (two-sided). **e.** Control (CTRL), SUN1, SUN2, NUP153
924 and RNF4 siRNAs (n \geq 4). **f.** CTRL, SUN1 and double PER1+SUN1 and PER2+SUN1 siRNAs
925 (n=3). **g.** CTRL, PER2, SUN1 and double PER2+NUP153 and SUN1+NUP153 siRNAs (n=3).
926 **h.** CTRL, PER2, RNF4 and double PER2+RNF4 siRNAs (n=3).

927

928

929 **Figure 6. The Circadian rhythm regulates TC-DSB targeting to nuclear envelope and**
930 **RAD51 loading**

931 **a.** γ H2AX foci intensity, measured by high content microscopy, in DIvA cells after DSB
932 induction (+DSB 2h), in G1, S and G2 phases at different time points after dexamethasone
933 (Dex) treatment (synchronization of the circadian rhythm). Bars at the different time points are
934 colored according to the PER2 expression level (from highest in dark cyan, to lowest in white).
935 Data were normalized to the average. Mean and SEM (n = 3 biological replicates, with >3000
936 nuclei acquired per experiment) are shown. *P*, paired t-test (two-sided) was computed using
937 high PER time-points (28h, 30h, 32h) compared to low PER time-points (40h, 42h, 44h).

938 **b.** γ H2AX ChIP-qPCR performed in DIvA cells before (-DSB) and after DSB (+DSB)
939 induction at 28h and 40h after dexamethasone treatment (Dex) at three TC-DSBs (DSB1-3).
940 Data were normalized to a control location devoid of DSB. Mean and SEM for n=4 biological
941 replicates. *P*, paired t-test (two-sided).

942 **c.** LaminB1 ChIP-qPCR performed in DIvA cells before (-DSB) and after DSB induction
943 (+DSB) at 28h and 40h after dexamethasone (Dex) treatment at four TC-DSBs (DSB1-4) and
944 DSB5 (DSB in silent locus). Data were normalized to a control location devoid of DSB and
945 expressed relative to the undamaged condition. Mean and SEM for n=5 biological replicates.
946 *P*, paired t-test (two-sided).

947 **d.** SUN1 ChIP-qPCR performed in DIvA cells before (-DSB) and after DSB induction (+DSB)
948 at 28h and 40h after dexamethasone (Dex) treatment at four TC-DSBs (DSB1-4) and DSB5.
949 Data are normalized to a control location devoid of DSB and further expressed related to data
950 obtained in the undamaged condition. Mean and SEM for n=3 biological replicates. *P*, paired
951 t-test (two-sided).

952 **e.** Number of PLA foci (γ H2AX-LaminB1) per nucleus in DIvA cells before (-DSB) and after
953 DSB induction (+DSB) at 28h and 40h after dexamethasone (Dex) treatment. Data were
954 normalized to the untreated samples. Mean and SEM (n=3 biological replicates) are shown. *P*,
955 paired t-test (two-sided).

956 **f.** RAD51 ChIP-qPCR performed in DIvA cells before (-DSB) and after DSB (+DSB) induction
957 at 28h and 40h after dexamethasone (Dex) treatment at four TC-DSBs (DSB1-4) and two
958 NHEJ-DSBs (DSB5-6). Data were normalized to a control location devoid of DSB and
959 expressed relative to DSB4-28h. Mean and SEM for n=6 biological replicates. *P*, paired t-test
960 (two-sided).

961 **g.** γ H2AX foci mean area, measured by high content microscopy, in DIvA cells after DSB
962 induction (+DSB 2h), in G1, S and G2 phase at different time points after dexamethasone (Dex)
963 treatment. Data were normalized to the average. Mean and SEM (n=3 biological replicates) are
964 shown. *P*, paired t-test (two-sided) was computed using high PER time points (28h, 30h, 32h)
965 compared to low PER time points (40h, 42h, 44h)..

966 **h.** DSB responsive genes expression was measured by RT-qPCR before (-DSB) and after
967 (+DSB) DSB induction in DIvA cells at 28h and 40h after dexamethasone treatment. cDNA
968 level of two D-compartment DSB responsive gene (*RNF19B* and *PLK3*), two non-D
969 compartment DSB responsive genes (*PPM1D* and *SLC9A1*) and two control genes not regulated
970 post DSB induction (*LPHN2*, *UTP18*) are shown. Mean and SEM for n=4 biological replicates.
971 *P*, paired t-test (two-sided).

972 **i.** Model. During the day (PER phase), PERIOD proteins are recruited at DSBs occurring in
973 transcribed loci (TC-DSBs). This triggers the targeting of the TC-DSBs to the NE and their
974 tethering to SUN1 and the Nuclear Pore Complex, further ensuring RAD51 loading and HR
975 repair. During the night (BMAL1 phase), in absence of PER1/2, impaired TC-DSB anchoring

976 to the NE leads to impaired RAD51 loading, and enhanced DSB clustering and D-compartment
977 formation.

978

979

980 **Methods**

981

982 **Cell culture and treatment**

983 U2OS, DIvA (AsiSI-ER-U20S)²⁰, AID-DIvA (AID-AsiSI-ER-U20S)⁸, 53BP1-GFP DIvA⁷³,
984 hTERT RPE1 and RPE-DIvA (mAID-AsiSI-ER-RPE1) cells were grown in Dulbecco's
985 modified Eagle's medium (DMEM) supplemented with 10%SVF (Invitrogen), antibiotics and
986 either 1 μ g/mL puromycin (DIvA cells) or 800 μ g/mL G418 (AID-DIvA cells) or both
987 puromycin and G418 (53BP1-GFP DIvA) or 10 μ g/ml Blasticidin (RPE-DIvA) at 37°C under
988 a humidified atmosphere with 5%CO₂. The cell lines were regularly checked for mycoplasma
989 contamination. For AsiSI-dependent DSB induction, DIvA cell lines were treated with 300nM
990 4-hydroxytamoxifen (OHT) (Sigma, H7904) for 4h (unless otherwise indicated). For DSB
991 induction with etoposide (Sigma, E1383), U2OS cells were treated with 0,5 μ M etoposide for
992 4h, dexamethasone-synchronized cells were treated with 1 μ M etoposide for 2h and hTERT
993 RPE1 cells were treated with 1 μ M etoposide for 4h. For DSB induction with doxorubicin
994 (Sigma, D1515), U2OS cells were treated with 0,1 μ M doxorubicin for 4h. For DDR kinase
995 inhibition, DIvA cells were pretreated for 1h and during subsequent DSB induction with either
996 20 μ M ATMi (KU-55933 from Sigma, SML1109), 2 μ M ATRi (ETP-46464 from Sigma,
997 SML1321) or 2 μ M DNAPKi (NU-7441 from Selleckchem, S2638). To stop inducing AsiSI-
998 DSBs, AID-DIvA cells were washed twice in pre-warmed PBS after OHT treatment and further
999 incubated with 500 μ M auxin (IAA) (Sigma, I5148) for 2h (unless otherwise indicated). For
1000 circadian rhythm synchronization, cells were incubated for 1h with 500nM dexamethasone

1001 (Dex) Sigma, D4902), then the medium was replaced (time = 0h). Dex treatment was done
1002 every 2h during 24h and the DSB induction was started for all synchronized cells at the same
1003 time, 24h after the last Dex treatment, to obtain a full period circadian rhythm (analyses are
1004 shown from 24h to 46h post-Dex). To induce DSBs, synchronized cells are treated during 2h
1005 or 4h surrounding the synchronization timepoint (e.g., from 23h to 25h after Dex for a 2h
1006 treatment corresponding at the synchronized time = 24h).

1007

1008 **RPE-DIVA cell line generation**

1009 ***Generation of mAID-AsiSI expression vectors***

1010 *pLV-OsTIR1-2Myc-T2A-mAID-HA-ER-NLS-AsiSI-P2A-PuroR*. The lentiviral vector allowing
1011 the coexpression of (i) the AsiSI restriction enzyme amino-terminally fused to a mini-auxin
1012 inducible degron (mAID)⁷⁴, a human influenza hemagglutinin (HA) tag, a modified estrogen
1013 receptor ligand binding domain (ER) and a nuclear localization signal (NLS) of SV40 large T
1014 antigen, (ii) the Myc-tagged rice F-box protein TIR1, and (iii) an antibiotic resistance selectable
1015 marker, was generated from the previously described pLV3 plasmid⁷⁵ by the following
1016 sequential modifications. First, a coding sequence for the T2A self-cleaving peptide was
1017 inserted between the Kpn2I and MluI restriction sites using pre-annealed T2A-F and T2A-R
1018 oligonucleotides. The mAID cDNA was then PCR-amplified using mAID-F and mAID-R
1019 primers and the pAID1.1-N plasmid (BioROIS, Japan) as a template, and inserted between
1020 XmaI and EcoRI restriction sites of the previous plasmid. A P2A cassette encoding the self-
1021 cleaving peptide (pre-annealed P2A-F and P2A-R oligonucleotides) was further inserted
1022 between MluI and EcoRI sites. Next, a cDNA fragment coding for puromycin-resistance was
1023 amplified by PCR with primers Puro-F and Puro-R, and added by Hot-Fusion⁷⁶ between EcoRI
1024 and NdeI restriction sites. The HA-ER-NLS-AsiSI coding sequence was then PCR-amplified
1025 from a previously described pBabe-Puro-HA-ER-NLS-AsiSI vector²⁰ with primers AsiSI-F and

1026 AsiSI-R and inserted by Hot-Fusion between BamHI and MluI restriction sites. Finally, the
1027 OsTIR1-2Myc coding sequence was amplified by PCR (primers TIR1-F and TIR1-R) from a
1028 synthetic DNA construct with optimized codons and inserted by Hot-Fusion at the MssI site.
1029 *pLV-OsTIR1-2Myc-T2A-mAID-HA-ER-NLS-AsiSI-P2A-BSD*. As hTERT RPE1 are already
1030 resistant to puromycin, puromycin-resistance gene was switched to blasticidin-resistance by
1031 NEBuilder HiFi DNA Assembly strategy. Amplification of pLV-OsTIR1-2Myc-T2A-mAID-
1032 HA-ER-NLS-AsiSI-P2A-BSD was done by PCR using F1_fwd, F1_rev, F2_fwd, F2_rev,
1033 F3_fwd, F3_rev primers. Coding sequence for blasticidin resistance was amplified from
1034 pCRIS-PITCHv2_BSD_dTAG plasmid (Addgene, #9179) using primers BSD_fwd and
1035 BSD_rev. PCR were performed using PrimeSTAR Max DNA Polymerase (Takara, ref R045A).
1036 0.1pmol of each fragment were then assembled for 1h at 50°C using NEBuilder HiFi DNA
1037 Assembly master mix from the NEBuilder HiFi DNA Assembly Cloning Kit (NEB, ref
1038 E5520S). Reaction products were amplified in provided bacteria and purified using QIAprep
1039 Spin Miniprep Kit.

1040 The intermediate and final constructs were checked by sequencing (Eurofins Genomics,
1041 Ebersberg, Germany). All restriction and modification enzymes were purchased from
1042 ThermoFisher Scientific (Illkirch, France). Oligonucleotides were from Eurofins Genomics.
1043 Production of lentiviral particles in HEK-293T cells and transduction of cells were performed
1044 as previously described⁷⁷.

1045 ***Generation of RPE-DIVa cell line***

1046 3.10⁵ cells were infected with lentiviral particules in DMEM, Hepes pH 7.4 10mM and
1047 polybrene 8μg/ml. Media was changed 18h after and transduced cells were selected with
1048 12μg/ml blasticidin for 10 days. Clones were isolated and selected according to γH2AX and
1049 AsiSI staining by immunofluorescence, and survival after DSB induction by 300nM OHT
1050 treatment for 4 hours.

1051

1052 **Multi-output screen methodology**

1053 Each of the 130 SMARTpool siRNAs from the TC-DSBR-focused siRNA library (Extended
1054 Data Table 1) was transfected in 10^6 AID-DIVa cells as described below (siRNA and plasmid
1055 transfection section), always including a negative (CTRL) and a positive (SETX) control
1056 siRNAs. Transfected cells were plated (i) in 96-well Cell Carrier Ultra plates (20.000 cells/well
1057 in triplicates per condition) for γ H2AX foci analysis (intensity and area) with quantitative high
1058 throughput imaging as described below (High-Content microscopy and Immunofluorescence
1059 sections); (ii) in 96-well plates (1000 cells/well in quadrupletes per condition for cell survival
1060 analysis as described below (WST-1 cell survival assay section); and in 10cm diameter dish for
1061 genomic DNA extraction and translocation frequency analysis as described below (DSB-
1062 induced rearrangement /Translocation assay section). All data from these different outputs post-
1063 DSB induction were expressed normalized to the negative control siRNA (CTRL) and
1064 compared to the positive control siRNA (SETX). For the 130 genes of interest, each measured
1065 variable (“ γ H2AX.foci Intensity”, “Clustering”, “Translocation” and “Survival”) was centered
1066 and scaled to obtain the z-score displayed in a heatmap. Genes were ordered according
1067 hierarchical clustering computed with Pearson correlation distance and ward.D clustering
1068 method. Then genes were divided in 2 groups based on the hierarchical clustering and means
1069 of z-scores for each group were computed and displayed in independent boxplot for each
1070 variable. Mean differences between groups were tested using student t-test.

1071 **siRNA and plasmid transfection**

1072 In U2OS and U2OS derived cell lines, siRNA transfections were performed using the 4D-
1073 Nucleofector and the SE cell line 4D-Nucleofector X kits (Lonza) according to the
1074 manufacturer’s instructions. Briefly, 1-10 μ L of 100 μ M annealed siRNA was transfected in 1-
1075 20 \times 10 6 cells with 20-100 μ L SE solution in Nucleocuvettes using the U2OS program CM-104.

1076 In RPE1 cell lines, 20nM of siRNA were transfected using Lipofectamine RNAiMAX reagent
1077 (Invitrogen 13778075) according to the manufacturer's instructions. Subsequent cell treatments
1078 were performed ~42-48h post-transfection. Most siRNAs used in this study were siGENOME
1079 SMARTpools (Dharmacon) which are a mixture of 4 individual siRNAs, see Extended Data
1080 Table 1. Individual siRNA sequences (Eurogentec) were used for SUN1, SUN2 or RBBP8/CtIP
1081 (Extended Data Table 1). For all experiments, the control siRNA (CTRL) was the siGENOME
1082 Non-Targeting Control siRNA Pool #2 (Dharmacon), except for Fig. 4h and Fig. 4i where the
1083 control siRNA used with SUN1 and SUN2 siRNAs was Ctrl1 (Extended Data Table 1). Plasmid
1084 transfections were performed using the 4D-Nucleofector and the SE cell line 4D-Nucleofector
1085 X S kit (Lonza) according to the manufacturer's instructions. Briefly, 0.5µg DNA was
1086 transfected in 10^6 cells with 20µL SE solution in Nucleocuvette strips using the U2OS program
1087 CM-104, and subsequent OHT treatments were performed 48h later. mCherry-LaminB1-10
1088 plasmid was a gift from Michael Davidson (Addgene plasmid #55069;
1089 <http://n2t.net/addgene:55069> ; RRID:Addgene_55069).

1090 **Immunofluorescence**

1091 Transfected 53BP1-GFP DIVA cells were grown on glass coverslips and fixed with 4%
1092 Paraformaldehyde during 15min at room temperature. After, 2 washes with PBS, the
1093 permeabilization step was performed by treating cells with 0,5%Triton X-100 in PBS for
1094 10min, then cells were blocked with PBS-BSA3% for 30min. Primary antibody against γ H2AX
1095 (Extended Data Table 2) was diluted in PBS-BSA3% and incubated with cells overnight at 4°C.
1096 After 3 washes for 5min in PBS-BSA3%, cells were incubated with anti-mouse secondary
1097 antibody (conjugated to Alexa594 or Alexa488, Invitrogen), diluted 1:1000 in PBS-BSA3%,
1098 for 1h at room temperature. After a Hoechst 33342 (Invitrogen) staining (5µg/ml for 5min at
1099 room temperature), Citifluor (AF1-25, Clinisciences) was used for coverslip mounting.

1100 **High content microscopy (QIBC)**

1101 U2OS, DIvA (AsiSI-ER-U20S)²⁰, AID-DIvA (AID-AsiSI-ER-Transfected or Dex-
1102 synchronized DIvA and U20S cells were plated in 96-well Cell Carrier Ultra plates (Perkin
1103 Elmer). Prior to the end of OHT, etoposide or bleomycin treatments, cells are treated with 10µM
1104 EdU (Invitrogen, C10340) at 37 °C for 15min. For γ H2AX staining, cells are fixed and
1105 permeabilized as described above. For RAD51 staining, buffer II pre-extraction (20mM NaCl,
1106 0.5% NP-40, 20mM HEPES at pH 7.5, 5mM MgCl₂, 1 mM DTT) was added to cells for 20min
1107 on ice followed by fixation in 4% Paraformaldehyde during 15min at room temperature and
1108 washed twice with PBS. Then EdU was labeled by Click-iT AlexaFluor 647 reaction
1109 (Invitrogen, C10340) according to the manufacturer's instructions (cells protected from light
1110 from now). Cells were washed twice for 5min in PBS-BSA3% and then blocked with PBS-
1111 BSA3% for 30min at room temperature. Primary antibodies targeting γ H2AX or RAD51
1112 (Extended Data Table 2) were diluted in PBS-BSA3% and incubated with cells overnight at
1113 4°C. After 3 washes of 3min in PBS-BSA3%, cells were incubated with anti-mouse Alexa 488
1114 secondary antibody (Invitrogen) diluted 1:1000 in PBS-BSA3%, for 1h at room temperature.
1115 After 3 washes of 3min in PBS, nuclei were labeled with 5µg/ml Hoechst 33342 (Invitrogen)
1116 for 30min at room temperature. The cells were then washed twice with PBS and stored at 4°C.
1117 γ H2AX foci were further analyzed with an Operetta CLS High-Content Imaging System
1118 (Perkin Elmer) and Harmony software (version 4.9). For quantitative image analysis, ~20-80
1119 fields per well were acquired with a 20X (for γ H2AX circadian synchronization) or 40X
1120 objective lens to visualize >3000 cells per well in triplicate. Subsequent analyses were
1121 performed with Columbus software (version 2.8.2). Briefly, the Hoechst-stained nuclei were
1122 selected with B method, and the size and roundness of nuclei were used as parameters to
1123 eliminate false positive compounds. Then, the Find Spots D method was used (Detection
1124 sensitivity =0.2-0.4; Splitting coefficient =1; Background correction =0.5) to determine the

1125 number, mean area and intensity of repair foci in each nucleus. For cell cycle analysis, the sum
1126 of the Hoechst intensity and the mean of the EdU intensity were plotted in order to select G1,
1127 S, and G2 cells.

1128 Determination of the number (y axis) and size of γ H2AX foci (mean area on the x axis) in each
1129 nucleus has been used to infer DSB clustering (>8000 nuclei analyzed per sample) and the
1130 resulting scatter plots are divided into four quadrants on the basis of the medians^{10,11}.
1131 Percentages of cell populations with low number of γ H2AX foci of large size (lower right-side
1132 area of the scatter plot), called “cluster positive cells”, or with high number of γ H2AX foci of
1133 small average size (upper left area of the scatter plot), called “cluster negative cells”, are
1134 determined.

1135 **DSB- induced rearrangement/translocation assay**

1136 AID-DIVa cells were treated as indicated and DNA was extracted using the DNeasy kit
1137 (Qiagen). Illegitimate rejoining frequencies between different AsiSI sites, *t*(*MIS12;TRIM37*)
1138 and *t*(*LINC00217;LYRM2*), were analyzed by qPCR (in 3-4 replicates) using primers referenced
1139 in Extended Data Table 1²³. Results were normalized using two control regions (Norm1 and
1140 Norm17) both far from any AsiSI sites and γ H2AX domains (primers in Extended Data Table
1141 1). Normalized translocation frequencies were calculated using the Bio-Rad CFX Manager 3.1
1142 software.

1143 **WST-1 cell survival assay**

1144 Transfected AID-DIVa cells were plated in 96-well plates for each of the 3 conditions: -DSB,
1145 +DSB, +DSB+repair. 48h later, cells were treated or not with OHT for 4h and further incubated
1146 or not with IAA for 4h. Eight days after DSB induction, the medium is replaced by a mix of
1147 100 μ l warmed medium + 10 μ l WST-1 ready-to-use solution per well and the cells were
1148 incubated for 2h at 37°C. The tetrazolium salts from Premix WST-1 Cell Proliferation Assay

1149 System (TAKARA) are cleaved by mitochondrial dehydrogenase in viable cells to produce
1150 formazan dye, which is quantified by measuring its absorbance at 450nm (Multiskan GO
1151 Microplate Spectrophotometer from Thermo Fisher Scientific). The percentage of viable cells
1152 is normalized to the undamaged cells and compared to the control condition.

1153 **Clonogenic assays**

1154 Transfected AID-DIVa cells were seeded, in duplicate, at a clonal density in 10cm diameter
1155 dishes and, 48h later, were treated or not with 4OHT for 4h and washed twice in pre-warmed
1156 PBS and further incubated with auxin (IAA) for another 4h when indicated. Then, the medium
1157 was replaced for all cell dishes. After 8 days at 37°C under a humidified atmosphere with
1158 5%CO₂, cells were washed in PBS and stained with crystal violet (Sigma, V5265). Images of
1159 stained colonies were obtained using the White Sample Tray for the ChemiDoc Touch Imaging
1160 System (Bio-Rad) and colonies were counted using the Spot Detector plugin of Icy software,
1161 Version 2.0.2.0 (icy.exe program). Only colonies containing more than 50 cells were scored.
1162 The same protocol was applied to transfected U2OS and hTERT RPE1 cells treated with
1163 etoposide or doxorubicin.

1164 **Western blots**

1165 DIVa cells were incubated in RIPA buffer (50mM Tris pH8.0, 150mM NaCl, 0.5% sodium
1166 deoxycholate, 1% NP-40, 0.1% SDS) on ice for 20 min. Samples were further incubated with
1167 250 units of Benzonase (Sigma, E1014) per million of cells for 10 min at room temperature,
1168 then centrifuged at 13,000 rpm for 10 min at 4°C. The supernatants, containing soluble protein
1169 extracts, were then mixed with SDS loading buffer and reducing agent, and incubated 10 min
1170 at 70°C. Electrophoreses were performed using 4–12% NuPAGE Bis-Tris gels (Invitrogen) and
1171 semi-dry western blotting on nitrocellulose membranes (Bio-Rad) was done with the Trans-
1172 Blot Turbo System (Bio-Rad) according to the manufacturer's instructions. Membranes were

1173 incubated in TBS containing 0.1% Tween 20 (Sigma, P1379) and 4% BSA during 1h at room
1174 temperature for blocking, followed by overnight incubation at 4 °C using primary antibody
1175 diluted in TBS-Tween-4% BSA. The corresponding mouse or rabbit horseradish peroxidase-
1176 coupled secondary antibodies (Sigma, A2554 and A0545) were used at 1:10,000 to reveal the
1177 proteins, using a luminol-based enhanced chemiluminescence HRP substrate (Super Signal
1178 West Dura Extended Duration Substrate, ThermoScientific). Picture acquisition of the
1179 membranes was done using the ChemiDoc Touch Imaging System (Bio-Rad) and pictures were
1180 analyzed using Image Lab software (Bio-Rad). All primary antibodies used in this study are
1181 detailed in Extended Data Table 2. Note: although different conditions and several human PER1
1182 antibodies were tested, none of them resulted in a ~140kDa signal corresponding to the PER1
1183 protein on the western-blots.

1184 **RT-qPCR**

1185 Total RNA was extracted from U2OS and DIvA cell lines before and after DSB induction using
1186 homogenization with QIAshredder and the RNeasy kit (Qiagen) following the manufacturer's
1187 instructions. RNA was then reverse transcribed to cDNA using the AMV reverse transcriptase
1188 (Promega, M510F). qPCR experiments were performed to assess the levels of cDNA using
1189 primers referenced in Extended Data Table 1. cDNA levels were then normalized with GAPDH
1190 (Gene ID: 2597), TBP (Gene ID: 6908) and 18S (RNA18SN5, Gene ID: 100008588) cDNA
1191 levels using the CFX Manager 3.1 software (Bio-Rad).

1192 **Resection assay**

1193 Measure of resection was performed as described in⁵³ with the following modifications.
1194 Genomic DNA was extracted from transfected DIvA cells just after DSB induction using the
1195 DNeasy kit (Qiagen) without any vortexing step. 1 µg of DNA was incubated 20min at 37°C
1196 with 15 units of RNaseH1 (New England Biolabs) and first digested for 2h at 37°C with 35

1197 units of AsiSI restriction enzyme (New England Biolabs). Then, 250ng of DNA were further
1198 digested overnight at 37°C using 10 units of BanI restriction enzyme, that cuts at 200bp from
1199 the DSB1, or of BanII restriction enzyme, that cuts at 1122bp from the DSB7 (Extended Data
1200 Table 1). Both enzymes were heat inactivated for 20 min at 80°C. Digested and undigested
1201 samples were analyzed by qPCR (10ng/well) using primers in Extended Data Table 1. ssDNA%
1202 was calculated with the following equation: Percent of ssDNA= $1/((\text{PUISSANCE}(2;(Ct$
1203 $\text{Digested} - \text{Ct Non Digested}) - 1) + 0.5)) * 100$.

1204 **Proximity Ligation Assay (PLA)**

1205 PLA experiments were performed using Duolink® In Situ Detection assay from Sigma-Aldrich
1206 according to the manufacturer's instructions. Primary antibodies used for PLA are detailed in
1207 Extended Data Table 2.

1208 ***High throughput γH2AX-LaminB1 PLA.*** siRNA-transfected or Dexamethasone-synchronized
1209 cells were plated in 96-well Cell Carrier Ultra plates (Perkin Elmer). At the end of DSB
1210 inducing treatment, cells are treated with 10µM EdU (Invitrogen, C10340) for 15min. Cells are
1211 fixed with 4% paraformaldehyde during 15min at room temperature. Permeabilization step was
1212 performed by treating cells with 0,5% Triton X-100 in PBS for 5min. Then EdU was labeled
1213 by Click-iT Alexa488 reaction (Invitrogen, C10340) according to the manufacturer's
1214 instructions. Cells were blocked with 1 drop of blocking solution provided with the Duolink®
1215 PLA Probes (DUO92002 and DUO92004, Sigma-Aldrich) for 1h at 37°C in a humid chamber.
1216 Primary antibodies targeting γH2AX and LaminB1 were diluted in the antibody dilution buffer
1217 provided with the Duolink® PLA Probes and incubated with cells overnight at 4°C. After two
1218 5min washes in Duolink® In Situ Wash Buffer A (DUO82049, sigma-Aldrich), cells were
1219 incubated with anti-mouse plus and anti-rabbit minus probes for 1h at 37°C, under slow
1220 rotation. After two washes in wash buffer A for 5min, cells were incubated for 30min at 37°C

1221 in the ligation reaction mix from the Duolink® In Situ Detection Reagents Red (DUO92008,
1222 Sigma-Aldrich). The cells were washed again twice in wash buffer A for 5min and incubated
1223 for 1h40 at 37°C under slow rotation for the amplification step. Finally, after two 10min washes
1224 in wash buffer B (DUO82049, sigma-Aldrich), nuclei were stained in the staining solution from
1225 the Duolink® In Situ Microplate Nuclear Stain (DUO82064, Sigma-Aldrich) for 30min at 37°C
1226 and cells were kept in the Anti-Fade solution (DUO82064, Sigma-Aldrich) until image
1227 acquisition. For quantitative image analysis, images were acquired with a 40X objective lens to
1228 visualize >3000 cells per well in duplicate. Subsequent analyses were performed with
1229 Columbus software (version 2.8.2) to determine the numbers of PLA foci in each nucleus. G1,
1230 S and G2 nuclei were selected based on EdU and DAPI staining distribution in all cells.

1231 **53BP1-LaminB1 and γH2AX-LaminB1 PLA.** siRNA-transfected cells were seeded on 13mm
1232 coverslips and treated for 4h with 4OHT before fixation in 4%PFA. Slides were then processed
1233 as before, except that there were no EdU staining, and that at the end of the PLA procedure,
1234 after the two 10min washes in wash buffer B, cells were then washed for 1min in 0.01% wash
1235 buffer B and mounted on slides with Duolink® In Situ Mounting Medium with DAPI
1236 (DUO82040, Sigma-Aldrich). Image acquisition was done on Leica DM6000 at 40X objective
1237 lens to visualize >175 cells per experiment in triplicate. Subsequent analyses were performed
1238 with Cell Profiler software (version 4.2.4) to determine the numbers of PLA foci in each
1239 nucleus.

1240 **3D super resolution using Random Illumination Microscopy (RIM)**

1241 **3D RIM two cameras setup.** The 3D RIM home-made setup is coupled to an inverted
1242 microscope (TEi Nikon) equipped with 100x magnification, a 1.49 N.A. objective (CFI SR
1243 APO 100XH ON 1.49 NIKON) and two SCMOS cameras (ORCA-Fusion, Hamamatsu)
1244 mounted in an industrial apochromatic alignment module (abbelight SA). Fast diode lasers

1245 (Oxxius) with wavelengths centered at 488nm (LBX-488-200-CSB) and 561nm (LMX-561L-
1246 200-COL) are used for all experiments. The bandpass emission filters in front of the two
1247 respective cameras are FF01-514/30-25 for camera 1 and FF01-609/54-25 for camera 2. The
1248 binary phase modulator (QXGA fourth dimension) conjugated to the image plane combined
1249 with polarization elements are used to generate dynamic speckle on the object plane as
1250 described in⁴⁷. The synchronization of the hardware (Z-platform, cameras, microscope, laser
1251 and SLM) is performed by an improved version of the commercial software INSCOPER.

1252 ***Fixed 3D RIM acquisition and reconstruction.*** Two-color 3D RIM imaging was performed
1253 with the 3D RIM system. The acquisition of 40 planes was done sequentially with a 120nm step
1254 in the image plane. For each image plane, 400 speckles were used to increase the desired super-
1255 resolved 3D resolution (95nm,95nm,200nm). The image reconstructions were performed with
1256 the software (ALgoRIM^{https://github.com/teamRIM/tutoRIM}). The Wiener filter used is 0.01,
1257 the deconvolution parameter is 0.02 and the regularization parameter is 0.02 for the first channel
1258 images. The Wiener filter used is 0.02, the deconvolution parameter is 0.03 and the
1259 regularization parameter is 0.02 for the second channel images. The misalignment between the
1260 two cameras and the residual chromatic aberrations are corrected using the SVI (Scientific
1261 Volume Imaging) software.

1262 ***3D+t two colors RIM super-resolution acquisition and reconstruction.*** 3D+t RIM movies
1263 were performed on AID-DIVa cells expressing 53BP1-GFP and mcherry-LaminB1. 3D movies
1264 of 47min with 40sec intervals were made (60 times). The whole cell acquisition time was 6
1265 seconds with 48 random patterns optimized for live cells for each plane. Image reconstructions
1266 were performed with the software (ALgoRIM^{https://github.com/teamRIM/tutoRIM}). The
1267 Wiener filter used is 0.01, the deconvolution parameter is 0.151 and the regularization
1268 parameter is 0.08 for the first channel images. The Wiener filter used is 0.1, the deconvolution

1269 parameter is 0.25 and the regularization parameter is 0.08 for the second channel images. The
1270 misalignment between the two cameras and the residual chromatic aberrations are corrected
1271 using the SVI (Scientific Volume Imaging) software.

1272 **3D film editing.** Bleaching correction is performed after RIM reconstruction with the open-
1273 source FIJI 546 software (<https://imagej.net/software/fiji/>) based on an exponential FIT from
1274 the background. The FIJI 3D drift correction plugin is performed for 3D registration
1275 (https://github.com/fiji/Correct_3D_Drift). Rendering of 3D+t movies was performed with the
1276 VTK library implemented in ICY software (<https://icy.bioimageanalysis.org/>) from 3D CROP
1277 on 550 areas of interest. Chromatism correction was performed by Scientific Volume Imaging
1278 (SVI) software.

1279 **Colocalization analyses.** The colocalization analyzer from the Scientific Volume Imaging
1280 (SVI) software is used on fixed 3D RIM images to quantify the interactions of γ H2AX nanofoci
1281 with those of SUN1 and SUN2.

1282 **Quantitative immunocolocalization (ICQ).** The intensity correlation quotient was defined in⁷⁸
1283 by the following equation for each voxel "i":

$$1284 (I_i^{D1} - I_{avg}^{D1})(I_i^{D2} - I_{avg}^{D2})$$

1285 For a random or mixed interaction, this number will tend towards 0, and for a dependent
1286 correlation, it will tend towards +0.5. This parameter does not directly use the intensity of each
1287 pair of voxels and has the advantage of eliminating the bias towards particularly high or too
1288 low intensities.

1289 **Cross-correlation function CCF.** The Van Steensel cross-correlation function (VSCF) CCF is
1290 used to quantify interactions and has been described in⁷⁹. It is obtained by calculating the

1291 Pearson coefficient after shifting the second camera image over a distance of Δx voxels.
1292 Thresholding was carefully tailored for each image to reject the 10th percentile of the lowest
1293 intensity value for both channels. The CCF was measured with the x-shift set to 940nm without
1294 rotation and the resulting three graphs were averaged and plotted with a 95 percentil. The
1295 Pearson coefficient is the classic equation below for each voxel "i":

$$1296 P = \frac{\sum (I_i^{D1} - I_{avg}^{D1})(I_i^{D2} - I_{avg}^{D2})}{\sqrt{\sum (I_i^{D1} - I_{avg}^{D1})(I_i^{D2} - I_{avg}^{D2})}}$$

1297 with I_{avg}^{D1} and I_{avg}^{D2} the averages of camera 1 and camera 2 of the microscope.

1298 For better visualization of the shape of the CCF function for each condition, we normalized the
1299 CCF function between 0 and 1 with the following normalization calculation:

1300 $P_{(0,1)} = \frac{(P - P_{min})}{(P_{max} - P_{min})}$, for Figure 3i and 3k or $P_{(min)} = (P - P_{min})$ for Extended Data Figure 6e.

1301 Negative values for Δx indicate a shift in nm of the red image to the left, positive values indicate
1302 a shift to the right. Non-random overlap results in a peak at $\Delta x=0$ and non-random exclusion
1303 results in a dip at $\Delta x=0$. Uncorrelated distributions will not show any clear peak in the CCF.

1304

1305 **ChIP-qPCR, ChIP-seq and data analysis**

1306 **ChIP-qPCR.** ChIP experiments were performed in DIVA cells according to the protocol
1307 described in^{8,20} with 200 μ g of chromatin per immunoprecipitation. The quantity of primary
1308 antibodies used is detailed in Extended Data Table 2. qPCR experiments were performed on
1309 both IP and input samples to assess the percent of input DNA immunoprecipitated, using AsiSI-

1310 induced DSBs and primers referenced in Extended Data Table 1. When indicated in the figure
1311 legends, data are normalized to a control location devoid of DSB (Ctrl genomic locus) and could
1312 be further expressed related to data obtained at DSB4 or in undamaged condition.

1313 ***Library preparation and sequencing.*** Multiple ChIP experiment samples were pooled and
1314 sonicated for 15 cycles (30 sec on, 30 sec off, high setting) with a Bioruptor (Diagenode), then
1315 concentrated with a vacuum (Eppendorf). 10ng of purified DNA (average size 250–300bp) was
1316 used to prepare sequencing libraries with the Next Ultra II Library Prep Kit for Illumina (New
1317 England Biolabs) using the application note for “Low input ChIP-seq”, and subjected to 75bp
1318 single-end sequencing using Illumina NextSeq500 at the EMBL Genomics core facility
1319 (Heidelberg, Germany).

1320 ***ChIP-seq data processing.*** ChIP-seq data processing was performed as described²². In brief,
1321 raw sequencing reads were aligned using bwa (<https://bio-bwa.sourceforge.net/>) to the human
1322 reference genome (hg19) and then, were sorted, deduplicated, and indexed using samtools
1323 (<http://www.htslib.org/>). Bigwig coverage tracks were subsequently extracted from the
1324 processed bam files using bamCoverage from deepTools (HYPERLINK
1325 <https://deftools.readthedocs.io/en/develop/>), and were normalized by total read count to be
1326 used for downstream analyses.

1327 ***DSB Average profiles and boxplots.*** Differential coverage tracks representing the log2 ratio
1328 between damaged and undamaged ChIP-seq samples were created using the bamCompare
1329 function of deepTools on default settings. These bigwigs were then used as input for the
1330 computeMatrix function of deepTools to calculate the coverage at DSBs using 200 bins
1331 covering either 10kb or 1kb as indicated on Figures. These matrices were then processed using
1332 a custom script in R with ggplot2.

1333 **Peak calling.** Peak calling for ChIP-seq datasets (BMAL1, SUN1 and SUN2) was performed
1334 using *MACS2* using -q 0.1 for BMAL1 resulting in 1776 peaks, and -q 0.005 for SUN1 and
1335 SUN2 resulting in 27326 and 14571 peaks respectively. Endogenous DSBs were identified as
1336 described in ¹¹. In brief, peaks were called from untreated pATM-ChIP-seq data⁸⁰ using *macs2*,
1337 identifying 1,206 regions. A random set of regions was then generated from the *gkmsvm* R
1338 package.

1339 **Gene Ontology Analysis.** Genes for BMAL1 GO analysis were selected if the identified
1340 BMAL1 peak was within a genes body or within its promoter region. The subsequent gene list
1341 was used to perform gene ontology analysis using the *enrichGO* function
1342 from *clusterprofiler* in R.

1343 **Peak annotation.** The genomic locations of SUN1 and SUN2 peaks were identified by using
1344 the *ChIPseeker* package in R, specifically the *annotatePeak* function to annotate the regions
1345 and *plotAnnoPie* for subsequent visualization. To calculate the coverage of SUN1 at SUN2
1346 regions, the *computeMatrix* function of *deepTools* was used using 200 bins over a 10kb
1347 window. The matrix was then processed using a custom script in R with *ggplot2*.

1348

1349 **Hi-C and data analyses**

1350 **Hi-C libraries.** Hi-C experiments were performed in DIvA cells following transfection with
1351 CTRL or PER2 siRNAs and with or without DSB induction as described in⁸⁰. Briefly, 10⁶ cells
1352 were used per condition. Hi-C libraries were generated using the Arima-HiC+ for HiC (Arima
1353 Genomics) by following the manufacturer's instructions. DNA was sheared using the Covaris
1354 S220 to obtain an average fragment size of 350-400pb. Sequencing libraries were prepared on
1355 beads using the Next Ultra II DNA Library Prep Kit for Illumina and Next Multiplex Oligos

1356 for Illumina (New England Biolabs) following instructions from the Arima-HiC+ for HiC
1357 (Arima Genomics). Hi-C data were processed as described in^{25,80} see below.

1358 ***Hi-C heatmaps.*** Hi-C reads were mapped to hg19 and processed with Juicer v2.0 using default
1359 settings (<https://github.com/aidenlab/juicer>). Hi-C count matrices were generated using Juicer
1360 at multiple resolutions: 100kb, 50kb, 25kb, 10kb, 5kb and 1kb. Hi-C heatmap screenshots were
1361 obtained using Juicebox (<https://github.com/aidenlab/Juicebox/wiki/Download>).

1362 ***Aggregate Peak Analysis (APA).*** APA plots of inter- or intra-chromosomal interactions of
1363 DSBs and control regions were created using the APA program of Juicer tools (<https://github.com/aidenlab/juicer/wiki/APA>) with a 10kb resolution -/+ 100kb.
1364

1365 ***Trans contact quantification.*** To determine inter-chromosomal interaction changes (in *trans*),
1366 we built the whole-genome Hi-C matrix for each experiment by merging all chromosome-
1367 chromosome interaction matrices using Juicer and R to obtain a genome matrix with 33kx33k
1368 bin interactions for 100kb resolution. Interactions between bins inside damaged TADs
1369 (240X240 for the 80 best-induced AsiSI DSBs) were extracted and counted for each condition,
1370 then log2 ratio was calculated on normalized count (cpm), and plotted as boxplots or heatmaps
1371 (https://github.com/LegubeDNAREPAIR/ATMcompD/blob/main/scriptR/Heatmap_D_trans.R).
1372

1373 ***A/B compartment.*** To identify A and B main chromosomal compartments, the extraction of the
1374 first Eigen vector of the correlation matrix (PC1) was done on the Observed/Expected matrix
1375 at 500kb resolution using juicer eigenvector command. The resulting values were then
1376 correlated with ATAC-seq signal in order to attributes positive and negative values to the A
1377 and B compartment, respectively, on each chromosome. The Observed/Expected bins were then
1378 arranged based on the PC1 values and aggregated into 21 percentiles, to visualize A-B

1379 interactions on the siPER2 and siCTRL experiments (saddle plots), and differences were
1380 computed between PER2 and control conditions for each percentile.

1381 **D-compartment.** For D-compartment identification, we retrieved the first component (PC1) of
1382 a PCA made on the differential observed over expected Hi-C matrix $\log_2 \left(\frac{\text{damaged}}{\text{undamaged}} \right)$ at 100kb
1383 resolution. Each matrix was extracted from the .hic files using Juicer and the ratio was
1384 computed bin per bin. Pearson Correlation matrices were then computed for each chromosome,
1385 and PCA was applied to each matrix. The first component of each PCA was then extracted and
1386 correlated with the position of DSBs. A PC1 showing a positive correlation with DSBs was
1387 then called D-compartment, and PC1 showing negative correlation with DSBs were multiplied
1388 by -1. We were able to extract the D-compartment on several chromosomes for +DSB/-DSB²⁵.
1389 D-compartment (first component of the PCA) was converted into a coverage file using
1390 rtracklayer R package. For analysis of DSB responsive gene expression by RT-qPCR, we used
1391 the previously determined D compartment genes as described in²⁵.

1392

1393 **Contact for Reagent and Resource Sharing**

1394 Further requests for reagents and resources should be asked to the lab PI, Gaëlle Legube
1395 (gaelle.legube@univ-tlse3.fr). DIVA cell lines are subjected to an MTA with the CNRS.

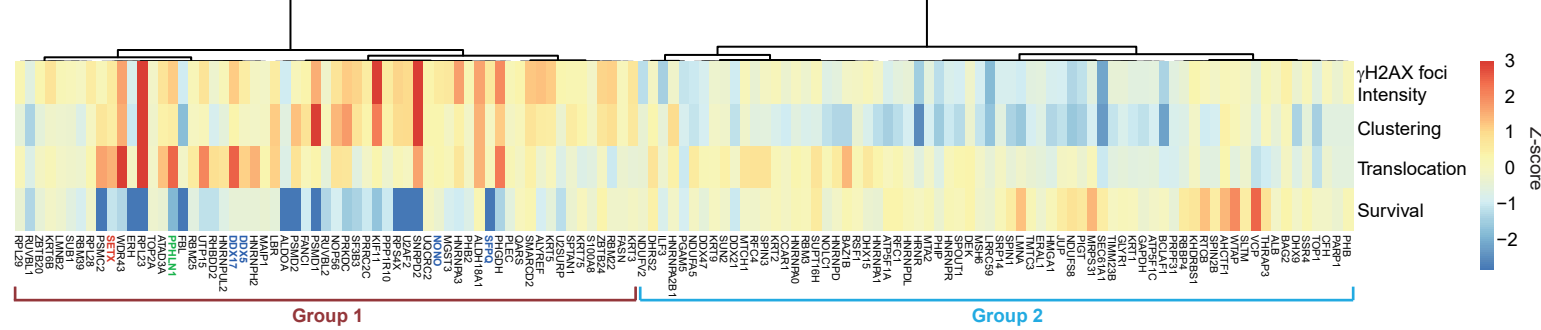
1396

Le Bozec et al, Figure 1

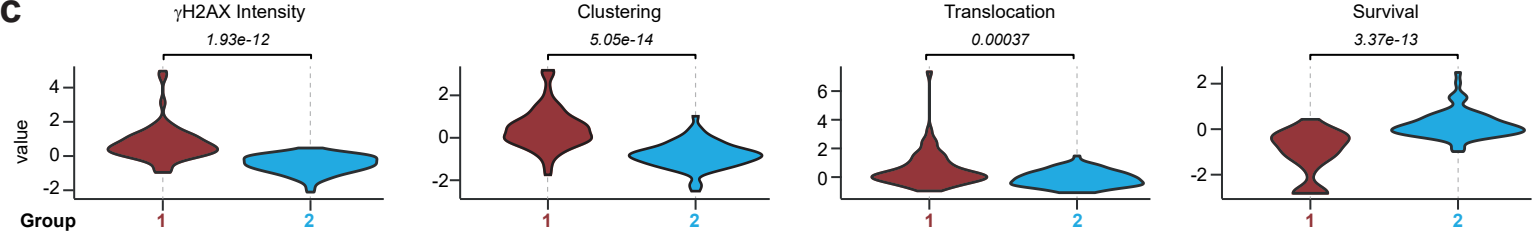
a



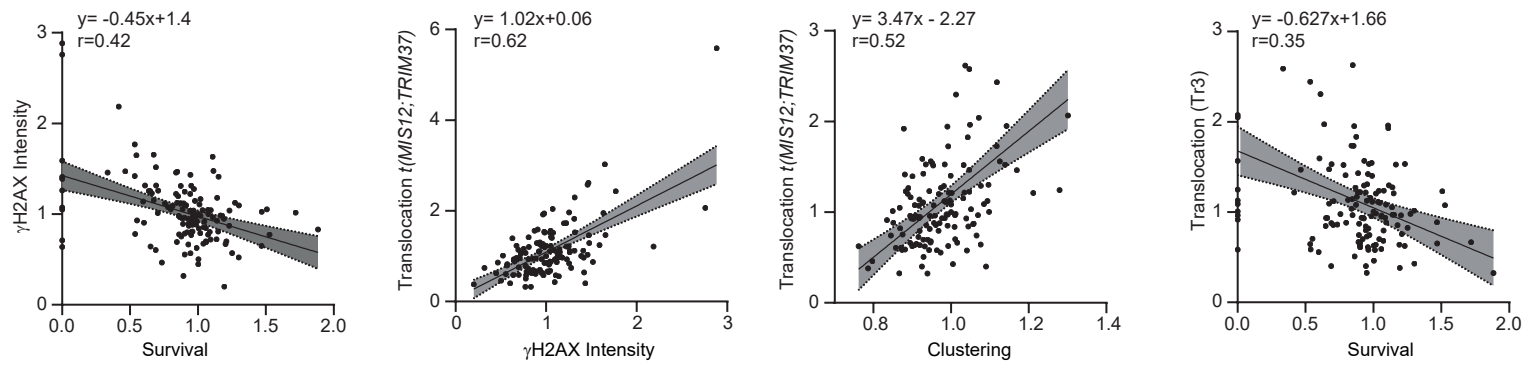
b

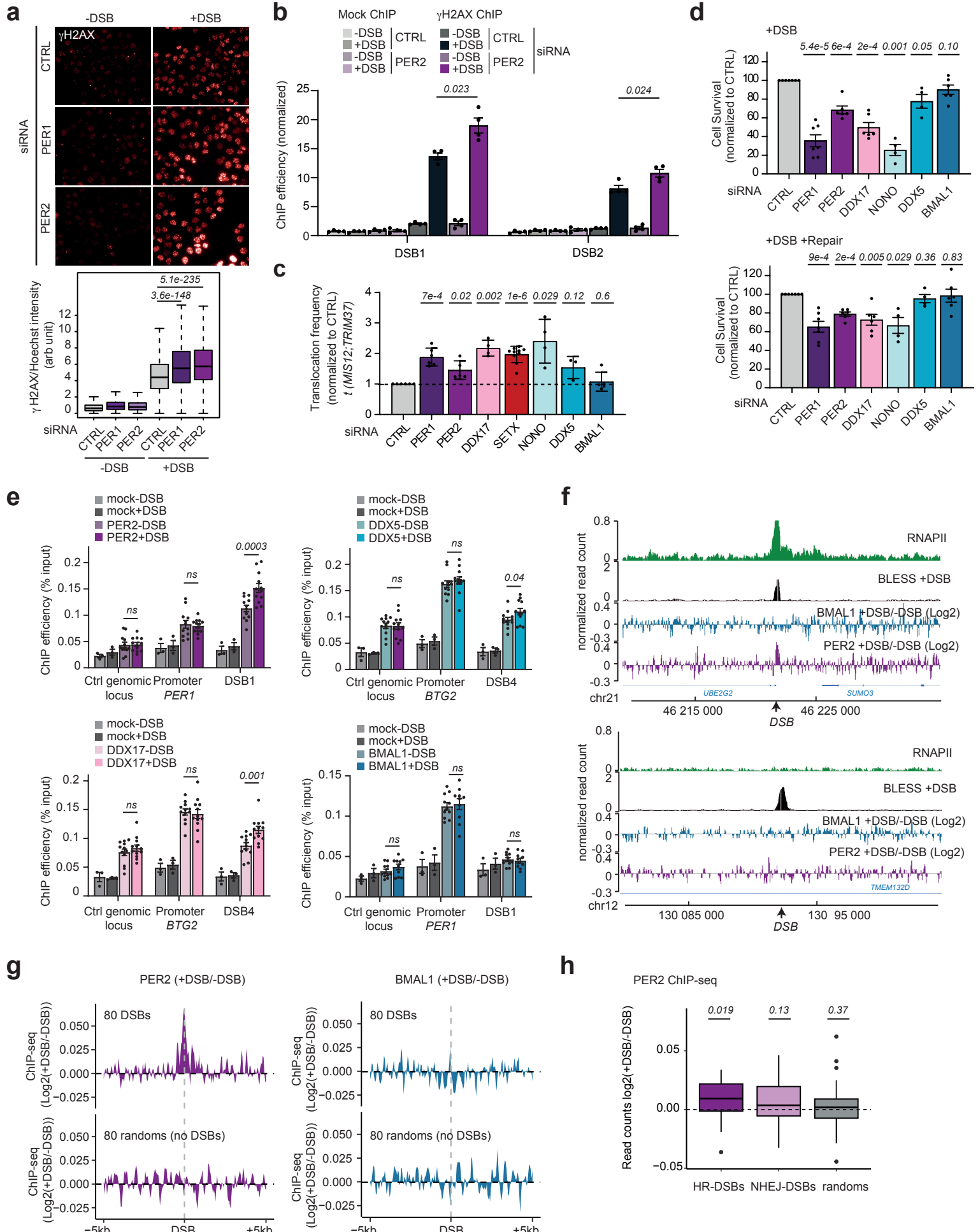


C

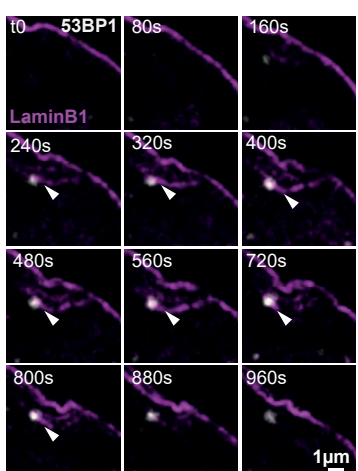


d

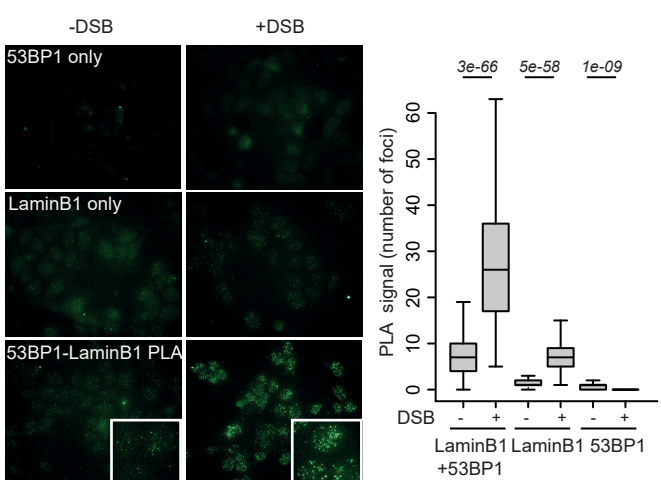




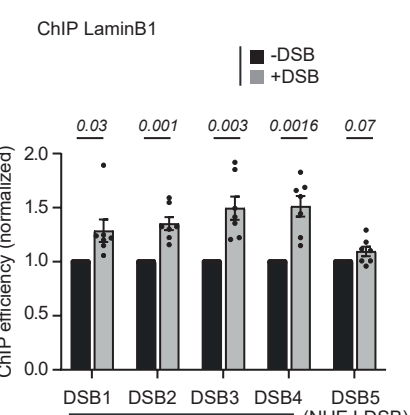
a



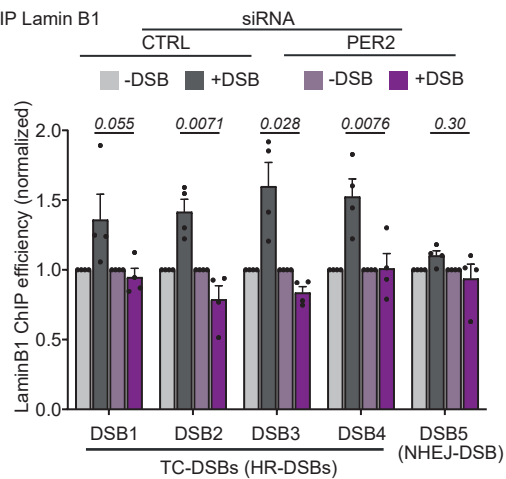
b



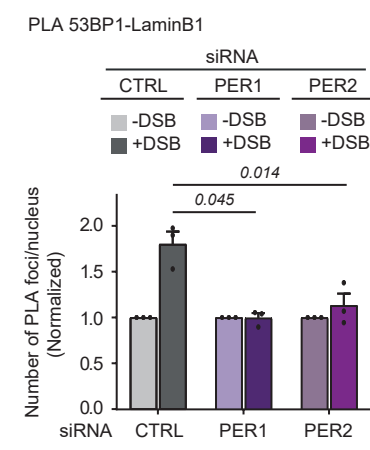
c



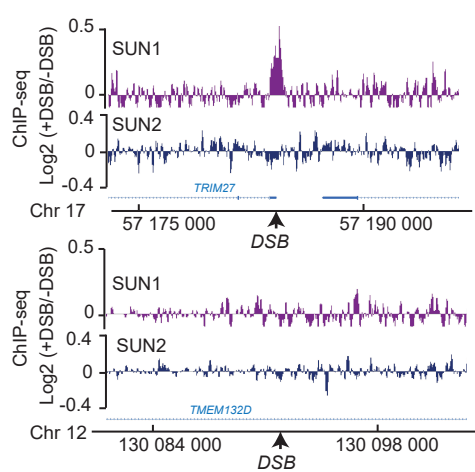
d



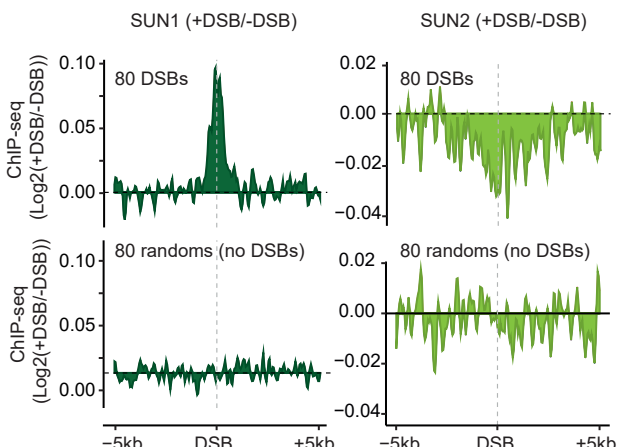
e



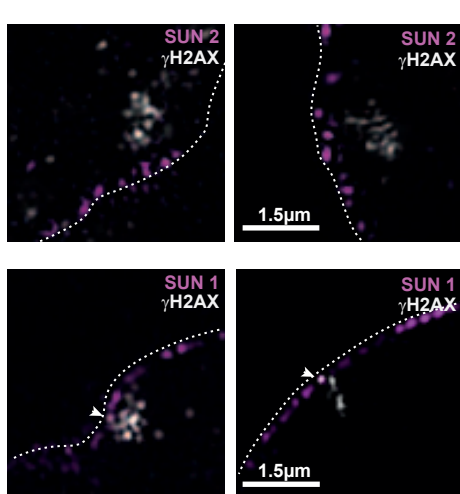
f



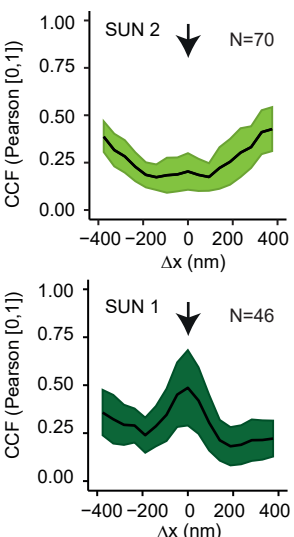
g



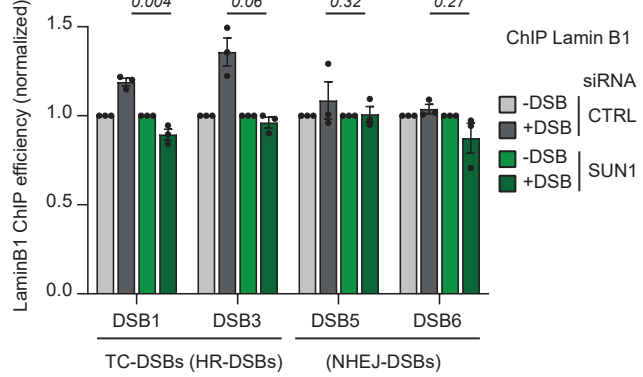
h



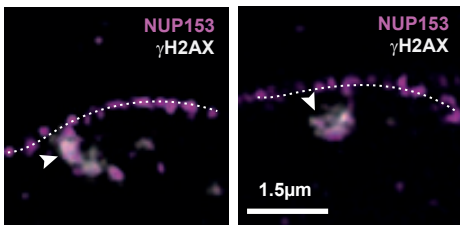
i



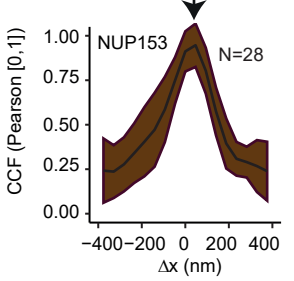
j



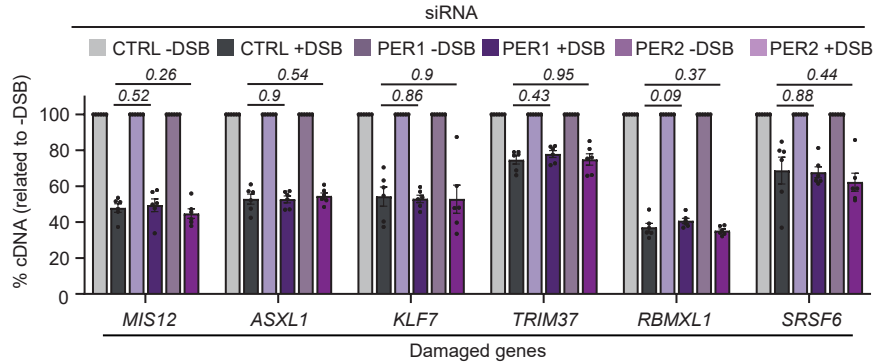
k



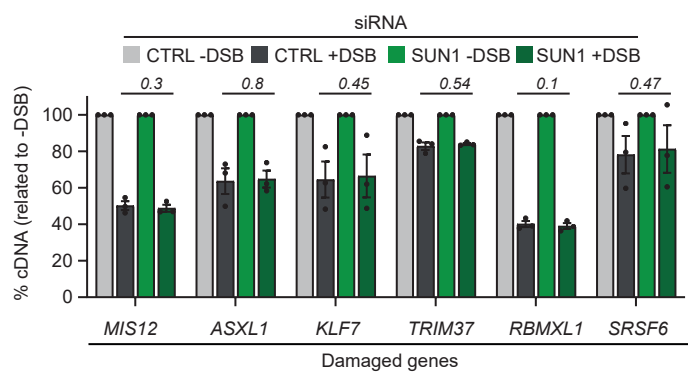
l



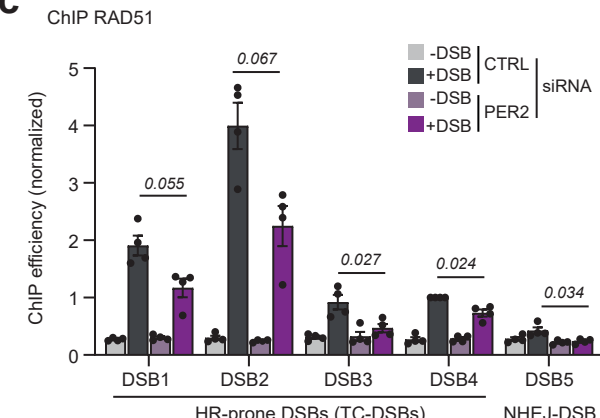
a



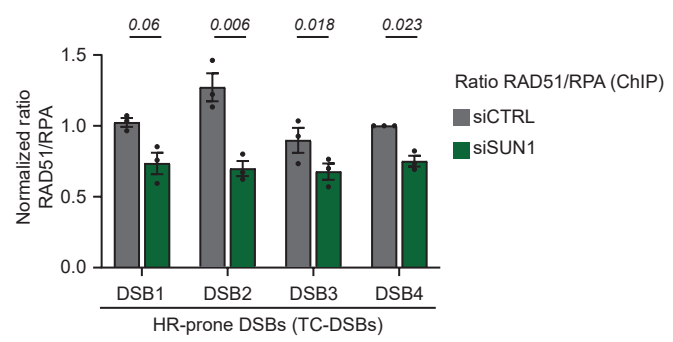
b



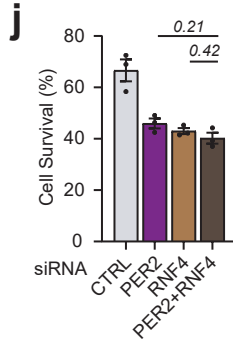
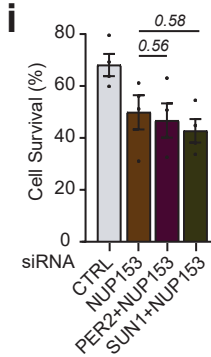
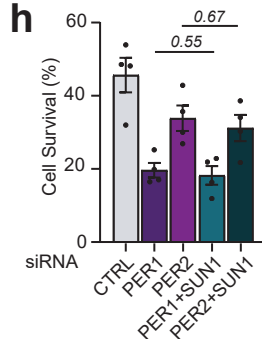
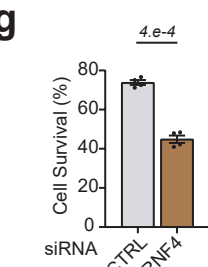
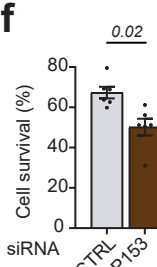
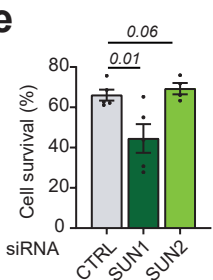
c



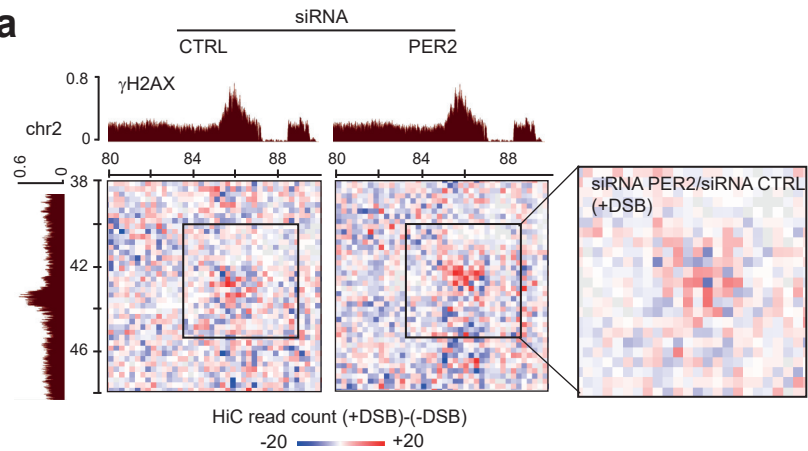
d



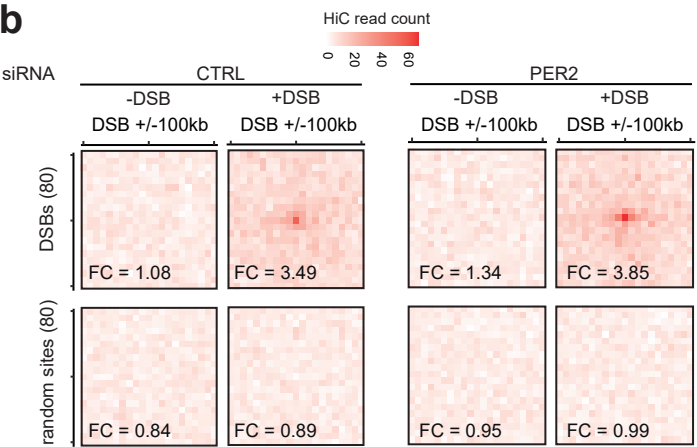
e



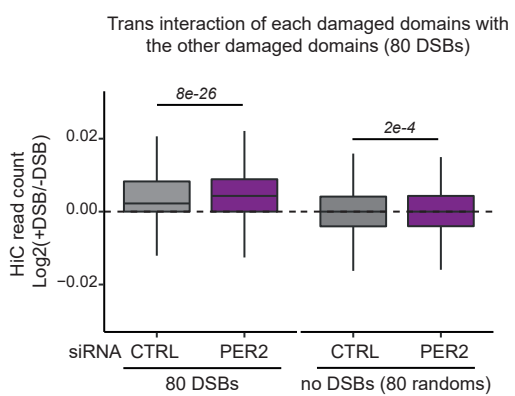
a



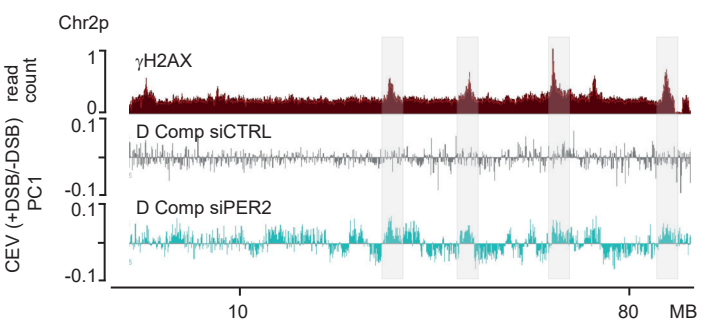
b



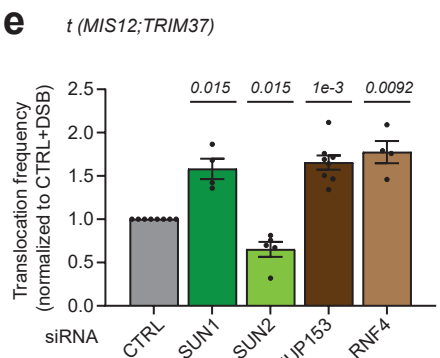
c



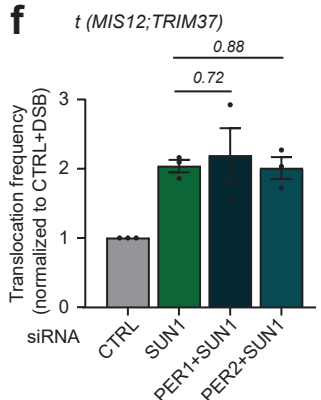
d



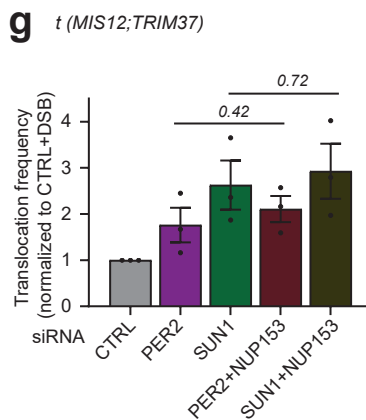
e



f



g



h

